Published in final edited form as:

Nature. 2019 May ; 569(7755): 222–228. doi:10.1038/s41586-019-1104-8.

The bone marrow microenvironment at single-cell resolution

Anastasia N. Tikhonova[1,*], **Igor Dolgalev**[1,12,*], **Hai Hu**[1], **Kishor K Sivaraj**[4], **Edlira Hoxha**[1], **Álvaro Cuesta-Domínguez**[5], **Sandra Pinho**[6], **Ilseyar Akhmetzyanova**[2], **Jie Gao**[3], **Matthew Witkowski**[1], **Maria Ruano Guillamot**[1], **Michael C. Gutkin**[8], **Yutong Zhang**[9], **Christian Marier**[9], **Catherine Diefenbach**[7], **Stavroula Kousteni**[5], **Adriana Heguy**[1,9], **Hua Zhong**[10], **David R. Fooksman**[2], **Jason M. Butler**[8], **Aris Economides**[3], **Paul S. Frenette**[6], **Ralf H. Adams**[4], **Rahul Satija**[11], **Aristotelis Tsirigos**[1,12], and **Iannis Aifantis**[1]

[1]Department of Pathology and Laura and Isaac Perlmutter Cancer Center, NYU School of Medicine, New York, NY 10016, USA

[2]Department of Pathology, Albert Einstein College of Medicine, 1300 Morris Park Avenue Forchheimer Building, Room 131 Bronx, NY 10461, USA

[3]Regeneron Genetics Center, Tarrytown, NY 10591, USA

[4]Department of Tissue Morphogenesis, Max Planck Institute for Molecular Biomedicine, and University of Münster, Faculty of Medicine, D-48149, Münster, Germany

[5]Department of Physiology and Cellular Biophysics, College of Physicians and Surgeons, Columbia University, New York, New York 10032, USA

[6]Ruth L. and David S. Gottesman Institute for Stem Cell and Regenerative Medicine Research, Albert Einstein College of Medicine, New York, NY 10461, USA

[7]Department of Medicine and Laura and Isaac Perlmutter Cancer Center, NYU School of Medicine, New York, NY 10016, USA

[8]Center for Discovery and Innovation, Hackensack University Medical Center, Nutley, NJ 07110, USA

[9]Genome Technology Center, Division of Advanced Research Technologies, NYU School of Medicine, New York, NY 10016, USA

[10]Department of Populations Health, Division of Biostatistics NYU School of Medicine, New York, NY 10016, USA

[11]New York Genome Center, New York, New York, USA

Corresponding authors: Anastasia.Tikhonova@nyumc.org. .

*These authors contributed equally

Contributions

A.N.T., I.D. and I.A. designed the study and prepared the manuscript. A.N.T. performed the majority of the experiments. I.D. performed all the computational analysis with guidance in the execution from R.S and A.T. J.G. generated mouse strains. H.H. and E.H. provided technical assistance with animal models. M.W. and S.P. performed differentiation assays with guidance in the execution from P.S.F. All microscopy was performed and interpreted by K.K.S., A.C., M.C.G., A.N.T. and I.A. with guidance from R.A., D.R.F., J.M.B, and S.K. Y.Z., C.M., and A.H. generated the scRNA-seq data. M.R.G. and C.D. assisted with transplantation assays. A.E., R.A. provided mouse strains and assisted with data analysis. H.Z. assisted with statistical analysis.

Competing financial interests. The authors declare no competing financial interests.

[12]Applied Bioinformatics Laboratories, NYU School of Medicine, New York, NY 10016, USA

Summary

The molecular complexity of the bone marrow (BM) microenvironment and its response to stress are incompletely understood, despite its key role in the regulation of hematopoiesis. Here we map the transcriptional landscape of BM vascular, perivascular, and osteoblast niche populations at single-cell resolution at both homeostasis and under stress hematopoiesis. This analysis revealed a previously unappreciated level of cellular heterogeneity within the BM niche, identified novel cellular subsets, and resolved cellular sources of pro-hematopoietic growth factors, chemokines, and membrane-bound ligands. Under conditions of stress, our studies revealed a significant transcriptional remodeling of these niche elements, including an adipocytic skewing of the perivascular cells. Among the stress-induced changes, we observed that vascular Notch ligand delta-like ligands (*Dll1,4*) were downregulated. In the absence of vascular *Dll4,* hematopoietic stem cells (HSC) prematurely induced a myeloid transcriptional program. These findings refine our understanding of the cellular architecture of the BM niche, reveal a dynamic and heterogeneous molecular landscape that is highly sensitive to stress, and illustrate the utility of single cell transcriptomic data in systematically evaluating the regulation of hematopoiesis by discrete niche populations.

Introduction

Hematopoiesis, the process of generating mature blood cells, is vital to carry out a variety of functions such as oxygen transport, immune defense, and tissue remodeling. This considerable undertaking is sustained by a rare population of self-renewing hematopoietic stem cells (HSCs), maintained in a specialized BM microenvironment composed of leptin receptor positive ($LepR^+$) mesenchymal stromal cells and vascular endothelial cells[1,2]. Osteoblasts have been proposed to support early lymphoid progenitor survival and commitment[3,4]. Additional signals provided by sympathetic nerve fibers[5,6], macrophages[7], megakaryocytes[8], and non-myelinating Schwann cells[9] also contribute to the HSC niche. Accumulating studies suggest further degree of cellular complexity of BM architecture, mediated through heterogeneity within vascular[10] and mesenchymal stem and progenitor cells (MSPCs)[11,12].

Hematopoiesis has to be controlled in a precise and rapid manner to meet the varying demands of homeostatic and stress conditions. Although our understanding of the BM niche has significantly evolved over the past decade, studies addressing the molecular heterogeneity and functional plasticity of the BM microenvironment have been limited, largely due to low frequencies of these populations in the BM and the technical challenges associated with their isolation. Here, by profiling 17,374 single BM niche cells, we identify previously unrecognized heterogeneity within the BM microenvironment and demonstrate how the microenvironment responds to acute BM stress at a single-cell level. We couple transcriptional profiling with novel fluorescent reporters and functional studies to demonstrate that vascular expression of the Notch receptor Dll4, identified by our single cell studies, suppresses premature upregulation of the myeloid program in HSCs.

Results

Transcriptomic profiling of the BM niche at single cell resolution

To reliably label the major BM niche subsets (Fig. 1a), we used lineage-specific Cre-transgenic mice crossed to a "knock-in" reporter strain, in which tdTomato is preceded by a "floxed" transcriptional stop at the *Rosa26* locus (*LoxP*-tdTomato). VEcad-cre; *LoxP*-tdTomato (VEcad-tdT) model labeled vasculature, the *Lepr-cre*;*LoxP*-tdTomato (Lepr-tdT) marked LepR$^+$ cells, and Col2.3-cre;*LoxP*-tdTomato (Col2.3-tdT) traced osteoblasts (Extended Data Fig. 1a). Reporter BM was enzymatic digested, CD45/Ter119^{lo}tdTomato$^+$ cells isolated (Extended Data Fig. 1b), and bulk mRNA sequencing (RNA-Seq) performed, confirming the presence of transcriptionally distinct populations (Extended Data Fig. 1c, d).

To study the transcriptomic diversity of BM niche populations, we conducted single-cell RNA-Seq (scRNA-Seq) of VEcad$^+$, LepR$^+$, and Col2.3$^+$ cells. We compared cells sorted from mice at steady-state and following acute stress induced by intraperitoneal 5-FU administration (Extended Data Fig. 2a). BM niche cells were isolated, mRNA libraries prepared (10x Genomics) and sequenced. Following quality filtering (see Methods), data was obtained for 18,339 cells. To correct for the observed batch effects between independent experiments (non-treated and PBS/5-FU treated), we used an "alignment" method[13] based on the canonical correlation analysis (CCA) (see Methods). The t-distributed stochastic neighbor embedding (tSNE) and graph-based clustering were employed to investigate cellular heterogeneity within the niche subsets. We removed 965 contaminating, mostly hematopoietic, cells and used the remaining 17,374 cells for the analysis (see Methods) (Fig. 3a, b).

To examine the baseline transcriptome of the BM niche, we surveyed only the cells under steady state conditions (n=9,622). Expression of genes associated with tissue-specific Cre expression (*Cdh5, Lepr,* and *Colla1*) confirmed a clear separation of input niche populations (Fig. 1b). We identified 2 endothelial, 4 perivascular, and 3 osteolineage subpopulations, as well as a small (n=70) proliferating cell cluster (Figs. 1c–d, Extended Data Fig. 1e). Our data is available for further exploration of cellular heterogeneity (http://aifantislab.com/niche). As the goal of our study was to broadly define BM niche architecture, we focused on the largest subpopulations.

Two major clusters were identified within the BM vasculature using integrated (Figs. 1d, 2a) as well as independent approaches (Extended Data Figs. 2b–d). To determine biomarkers for each subpopulation, pair-wise differential expression analysis for each cluster against all other clusters was performed. Branched networks of sinusoidal capillaries constitute the majority of blood vessels in the bone marrow, whereas the arteries contain comparably few side branches and are longitudinally aligned along the diaphysis[14]. Arterial-associated genes were expressed in cluster V1 (*Ly6a^{high}*; orange) and sinusoidal signature were specific to cluster V2 (*Stab2^{high};* blue) (Extended Data Fig. 3a)[15]. We performed BM immunofluorescence (IF), confirming arterial Sca1 (*Ly6a*), CD102*Icam2*) and Podxl (*Podxl*) expression (Extended Data Fig. 3b, c) and sinusoidal expression of Vegfr3[16] (*Flt4*) and CD54 (*Icam1*) (Extended Data Fig. 3d). Lama1 staining was used to specifically label BM vessels[17]. In agreement with expression data, flow cytometry analysis allowed arterial

identification by combining surface markers Sca1 (*Ly6a*), CD34 (*Cd34*) and Ly6C (*Ly6c1*) (Extended Data Fig. 3e).

The heterogeneity of the LepR$^+$ compartment has been an open question in light of its multilineage differentiation potential and mesenchymal stem cell (MSC) activity, as assayed by formation of fibroblastic colony-forming units (CFU-F)[18]. Integrated analysis identified four clusters within the LepR$^+$ compartment (Figs. 1c, d, 2b). Clusters P1 (*Mgp*^{high}; red) and especially P2 (*Lpl*^{high}; green) expressed adipogenesis-associated markers (Fig. 2b, Extended Data Fig. 4a). Analysis of the LepR$^+$ population alone confirmed clusters P1, P3 and P4 (Extended Data Fig. 2 e–g). Integrated analysis in the context of stress hematopoiesis revealed an additional P2 cluster (Figs. 1d, 3b), suggesting a poised pro-adipogenic state, rather than distinct progenitors. To validate potential biomarkers, we performed IF of Lepr-tdT femurs and found the sinusoidal capillaries covered with LepR$^+$Esm1$^+$ cells (specific to P1 and P2), whereas metaphysis and endosteum capillaries were LepR$^+$Esm1$^-$ (Extended Data Fig. 4b). Clusters P3 (Wif1^{high}; brown) and P4 (*Spp1*^{high}*Ibsp*^{high}; orchid) represented osteo-primed LepR$^+$ cells as they expressed progressively increasing levels of osteogenesis-associated genes (Fig. 2e). LepR$^+$ cells expressing P3/P4 specific markers CD200 (*Cd200*) and CD63 (*Cd63*) localized mainly to the trabecular portion of the bone (Extended Data Fig. 4c), consistent with their osteogenic signature. We detected high correlation between the human MSC gene signature of hCD45$^-$ CD271$^+$ BM cells[19] and clusters P1/P2 (Extended Data Fig. 4d). To functionally test *in vitro* stem cell capacity, we used surface markers to prospectively isolate LepR$^+$ cells (Extended Data Fig. 4e). Adipocyte-biased P1/P2 (Vcam1^{high}CD63^{low}) populations were significantly enriched in CFU-F and accounted for the majority of CFU-F activity of the total LepR$^+$ cells (Extended Data Fig. 4f).

The Col2.3$^+$ cells were transcriptionally split into three populations (Figs. 1c, d, 2c). Cluster O1 (*Col16a1*^{high}*Tnn*^{high}; gray) expressed high levels of osteocrin (*Ostn*), angiopoietin like 2 (*Angptl2*), as well as Del-1 (*Edil3*) that has been recently shown to regulate myelopoiesis[20] (Extended Data Fig. 5a). IF analysis of Col2.3-tdT femurs confirmed a subset of cells that co-expressed O1 marker Mmp14 (*Mmp14*) with tdTomato in the epiphysis (Extended Data Fig. 5b). Cluster O2 (*Fbn1*^{high}/*gf1*^{high}; moss) expressed osteogenic as well as chondrocyte-specific genes (Extended Data Fig. 5a). As it has been previously reported that hypertrophic chondrocytes co-express *Col10a1* with markers of osteoblastic differentiation[21], cluster O2 potentially represents cells undergoing osteogenic transdifferentiation (Fig. 1d, Extended Data Fig. 5a). Consistently, BM IF confirmed co-expression of O2-associated marker CD9 (*Cd9*) with tdTomato in the epiphysis (Extended Data Fig. 5c). Cluster O3 (*Bglap*^{high}*Car3*^{high}; olive) represented mature osteoblasts based on the highest expression of Col2.3 (*Col1a1*) and osteogenesis-associated genes (Fig. 2c, Extended Data Fig. 5a). BM IF confirmed co-staining of tdTomato with the biomarker Car3 (*Car3*) (Extended Data Fig. 5d). Additional smaller clusters were revealed through examination of the Col2.3$^+$ subset alone. Notably, aside from O1-O3 subsets, *Col1a1* was expressed in vascular endothelial (C4), glial (C5), and stromal-like (C6) cells (Extended Data Fig. 2h–j).

BM LepR$^+$ cells give rise to both osteoblasts and adipocytes[11]. As tSNE visualization does not maintain global structure of differentiation dynamics, we reconstructed the developmental trajectory to infer the relationship between LepR$^+$ P1-P4 cells and terminally

differentiated osteo populations (Fig. 2d). Pseudotime ordering revealed a transcriptional continuum of LepR$^+$ cellular states, with known adipogenic and osteogenic markers rising towards the opposite ends of this range (P1/P2 vs. P3/P4) (Fig. 2e).

To search for proliferating cells in the BM niche, we assessed cell-cycle associated genes, such as *Mki67* and found them confined to cluster C (magenta) (Fig. 1d, Extended Data Fig. 5e, f), comprised of all three examined niche populations (Extended Data Fig. 5g). This confirms that at steady state, the majority (>99%) of adult BM niche cells are not actively cycling. Collectively, these studies provide a detailed single-cell resolution map of the steady state quiescent BM microenvironment, allowing us to reveal cellular heterogeneity within each examined subset.

Single-cell profiling of BM niche-expressed factors able to regulate hematopoiesis

We next examined expression patterns of pro-hematopoietic factors[22] (Fig. 2f). We found that the vascular cells expressed the highest levels of angiogenin (Ang), delta-like Notch ligands (*Dll4* and *Dll1)*, and selectin E (*Sele*)[23]. Notably, within the vascular subset, arterial cluster V1 was enriched in SDF-1 (*Cxcl12*) and SCF (*Kitl*)[15]. LepR$^+$ clusters P1 and P2, in addition to expressing the highest levels of SDF-1 (*Cxcl12*), SCF (*Kitl*) and IL-7 *(Il7)*[24]*,* also represented a major source of IL-15 (*Il15*)[25], IL-34 (*Il34*), M-CSF (*Csf1*), BMP-4 (*Bmp4*)[26] as well as lymphocyte chemoattractant Ccl-19 (*Ccl19*) and monocyte chemoattractant Ccl-2 (*Ccl2*)[27], indicating that adipocytic-primed LepR$^+$ cells represent a major reservoir of pro-hematopoietic factors in the BM niche. Finally, the Col2.3$^+$ cluster O1 expressed Wnt5a (*Wnt5a*), previously demonstrated to maintain HSC quiescence[28], while cluster O2 represented the primary source of Igf-1 (*Igf1*), a critical factor in hematological malignancies[29] and B cell development[30]. Through the enhanced resolution afforded by scRNA-Seq, we were able to precisely define the cellular source and outline a distribution of pro-hematopoietic factors within the defined niche sub-populations.

Single-cell RNA-sequencing profiling of the BM niche in response to stress

Chemotherapy, frequently used for the treatment of leukemia, results in the ablation of rapidly dividing hematopoietic progenitor cells and induction of proliferation and differentiation of otherwise quiescent HSCs[31]. Myeloablation affects sinusoidal vessels[32] as well as stromal cells and causes an increase in the frequency of the BM adipocytes[33]. To assess the dynamic molecular and morphological changes of the BM niche under acute stress conditions, we administered a single dose of 5-fluorouracil (5-FU; 150mg kg^{-1})[34]. By day 5 (d5) following treatment, we detected a significant loss in BM cellularity, total counts of BM Lineage$^-$Sca-1$^+$CD117$^+$ (LSK) cells as well as BM vascular and perivascular populations (Extended Data Figs. 6a–c).

To track gene expression changes in the BM niche during stress hematopoiesis, we profiled 7,752 cells post 5-FU treatment (Fig. 3a). Our results revealed the formation of a novel adipo-primed cluster (P5, n=161; burnt orange) (Fig. 3b, Extended Fig. 6d) and a shift in cluster contribution throughout LepR$^+$ and Col2.3$^+$ populations (Fig. 3c). Specifically, LepR$^+$ cells underwent significant transcriptional reprogramming through the expansion of adipo-primed cluster P2. Overall, upon 5-FU treatment, we observed a significantly upregulation

of adipogenesis-related pathways and a global reduction in osteolineage-associated gene expression (Extended Data Figs. 6e, f). Two independent scRNA-seq experiments on VEcad$^+$ and LepR$^+$ populations showed comparable responses to 5-FU treatment, with a correlation coefficient of r=0.63 for vascular and r=0.88 for LepR$^+$ population for significantly altered genes, indicating comparable association between experiments (Extended Data Fig. 7). These results are consistent with the previously reported expansion of adipocytes following bone marrow insult[11,12].

An additional response to stress was an increase in cell proliferation across the niche subsets. Following myeloablation, 5.4% of cells were in the cycling cell cluster as compared to 0.7% at steady state (Extended Data Figs. 6g, h), potentially indicating initiation of a regeneration process.

We next examined 5-FU mediated changes of pro-hematopoietic factors (Fig. 3d). We detected upregulation of vascular *Ang,* perivascular *Il7* and *Bmp4,* and osteo *Wnt5a,* as well as downregulation of vascular Notch Delta ligands, *Dll4* and *Dll1,* adhesion molecule *Sele* and perivascular *Wnt4,* indicating changes in signaling strength of key pathways such as Wnt and Notch. Collectively, our studies define considerable molecular reprogramming of the BM microenvironment in response to chemotherapy.

Vascular endothelial niche cells represent the major source of Notch ligands *Dll4* and *Dll1* in the BM

Our analysis revealed that the Notch ligands *Dll1* and *Dll4* are specifically expressed in the VEcad$^+$ cells (Fig. 2f). RT-PCR analysis confirmed high expression of *Dll1* and *Dll4* in the vascular endothelial subset compared to perivascular and osteolineage cells, whereas *Jag1* expression was lower and comparable throughout vascular and perivascular populations (Extended Fig. 8a). Moreover, *Dll1* and *Dll4* expression was dynamically downregulated in response to stress (Fig. 3d). Targeting Notch receptor signaling in hematopoietic cells previously established critical roles of this pathway in normal hematopoiesis. However, the identity and roles of specific Notch ligands throughout the BM remain unclear[35,36], with the notable exception of Jag1, recently found to support HSC self-renewal[37].

To further map the BM Notch ligand expression, we generated Bacterial Artificial Chromosome (BAC) - carrying transgenic reporter mice co-expressing individual Notch ligands - *Dll1, Dll4* or *Jag1* – and the fluorescence marker mCherry (Fig. 4a). Using fluorescence microscopy, we observed *Dll4* and *Dll1* expression throughout the cortical thymic epithelium[38,39] and *Jag1* expression within the thymic medulla[40], consistent with previously published observations (Extended Fig. 8b). Flow cytometric analysis of the BM CD144$^+$ (VE-cadherin) vascular population within individual Notch ligand reporter strains confirmed high vascular endothelial expression of *Dll4* and intermediate levels of *Dll1* expression (Fig. 4b, Extended Data Figs. 8c, d). *In vivo* two-photon imaging and IF of *Dll4*-mCherry bones confirmed expression of *Dll4* throughout the BM vascular compartment (Fig. 4c, Extended Data Figs. 8e, g). *Dll1* was additionally expressed in a subset of NK1.1$^+$ hematopoietic cells (Fig. 4d, Extended Data Figs. 8f–j). Collectively, this data provides a comprehensive map of *Dll4* and *Dll1* expression throughout the BM.

Vascular Dll4 expression regulates HSC differentiation and lineage commitment

To further investigate a putative role of vascular Dll4 in normal hematopoiesis, we assessed the impact of vascular endothelial-specific deletion of *Dll4.* We crossed a vascular-specific, tamoxifen-inducible Cre strain (*Cdh5*-CreERT2) to mice harboring a conditional *Dll4 loss-of-function* allele (*Dll4*^{i3COIN}), termed VEc-*Dll4*^{i3COIN}. Following *Dll4* deletion throughout the VEcad^{+} vascular compartment, we detected a decrease in the frequency of Lin^{-}Sca-1^{low}CD117^{low}Flt3^{+}IL7Rα^{+} common lymphoid progenitors (CLPs) and an expansion of myeloid progenitor populations within the Lin^{-}Sca-1^{-}CD117^{+}FcγR^{+}CD34^{+} gate (GMP-gate), previously reported to contain mixed-lineage myeloid potential[41–43] (Extended Data Fig. 9a,b). Accordingly, we observed a loss of B220^{+} B cell and CD3^{+} T cell lymphoid populations and an expansion of the myeloid Gr1^{+}CD11b^{+} compartment in VEc-*Dll4*^{i3COIN} animals (Figs. 5a–c, Extended Data Fig. 9c, d). Interestingly, despite the loss of CLP cells, the deletion of vascular *Dll4* did not affect frequencies or numbers of Lin^{-}CD117^{+}Sca-1^{+}CD135^{+}IL7Rα^{-} lymphoid-primed multipotent progenitors (MPP4/LMPP)[44], considered to be upstream of the CLP subset (Extended Data Fig. 9h, i). Consistent with the loss of early lymphoid progenitors, we observed a significant loss of the thymic cellularity in VEc-*Dll4*^{i3COIN} animals and decrease in numbers of early thymic progenitors (ETP: CD4^{-}CD8^{-}CD25^{-}CD44^{+}CD117^{+}), but no evidence of specific developmental blocks in thymocyte differentiation (Extended Data Figs. 9e–g).

We detected no significant alterations in frequencies or numbers of phenotypic LT-HSCs (Lin^{-} CD117^{+}Sca-1^{+}CD150^{+}CD48^{-}) or multipotent progenitors (MPP2: Lin^{-}CD117^{+}Sca-1^{+}CD150^{+}CD48^{+} and MPP¾: Lin^{-}CD117^{+}Sca-1^{+}CD150^{-}CD48^{+}) in the absence of vascular *Dll4* (Extended Data Fig. 9h, i). IF analysis confirmed localization of CD150^{+}Lin^{-} hematopoietic stem progenitor cells (HSPCs) in the proximity of vasculature[45] in *mDll4-mCherry* animals (Extended Data Fig. 9j). To further define the impact of vascular *Dll4* deletion on the HSPC population, we performed scRNA-seq on HSPCs from control and VEc-*Dll4*^{i3COIN} animals. Following quality controls (see Methods), we profiled 21,116 HSPCs (Extended Data Fig. 9k). To assign cells to specific HSPC subsets (HSCs, MPP2–4), we scored individual cells by calculating a module score based on the average expression levels of the previously reported population-specific gene signatures[46] (Fig. 5e). Our analysis revealed a premature upregulation of the myeloid gene expression program[47] as early as the HSC stage, further preserved in all consecutive progenitor populations and a reduction of HSC enrichment (Extended Data Fig. 9l, m). Well-established myeloid-associated genes were ectopically overexpressed across all HSPC subsets (Fig. 5f). These results demonstrate a complete rewiring of the hematopoietic lineage commitment in the absence of the vascular Dll4, leading to a significant myeloid bias of all HSPC fractions and providing a molecular explanation for the phenotype of the VEc-*Dll4*^{i3COIN} animals.

Finally, we assessed the role of vascular endothelial-specific *Dll1* deletion on normal hematopoiesis, by combining Dll1-floxed alleles (*Dll1*$^{fl/fl}$) and VEcad-Cre to generate EC-specific *loss-of-function* mice (VEc-*Dll1*$^{fl/fl}$). We found no alterations in hematopoietic differentiation (Extended Data Fig. 10). Taken together, these results indicate that vascular Dll4, but not Dll1, is a key Notch ligand controlling early hematopoietic differentiation potential.

Discussion

A growing body of evidence proposes a departure from the traditional hierarchical model of hematopoiesis, suggesting instead a fluidity in the ability of each HSC to differentiate towards distinct lineages[48]. It is tempting to hypothesize that such plasticity is dictated by unique interactions between HSCs and the components of the microenvironment. Our results expand the understanding of the BM niche by presenting a detailed transcriptional blueprint of distinct vascular, perivascular, and osteolineage BM niche components.

Here we show that single-cell transcriptomic profiling can translate to novel mechanistic insights into the regulation of stem/progenitor cell differentiation. We match hematopoietic factors to their cellular sources and show that the loss of vascular endothelial-expressed Notch ligand Dll4 skews BM hematopoiesis toward a significant transcriptional reprogramming and myeloid priming of HSPCs. Future studies should investigate the functional consequences of niche heterogeneity on aberrant stem cell functions, such as immunodeficiency, hematopoietic malignancies, and aging. Targeting niche-associated factors could interfere with the disease initiation and progression, as it was recently shown by targeting vascular Cxcr4:Cxcl12 interactions in acute lymphoblastic leukemia[49,50].

Methods

Animals.

B6.FVB-Tg(Cdh5-cre)7Mlia/J (VEcad-Cre)[51], B6.129-Leprtm2(cre)Rck/J (Lepr-Cre)[52], and B6.Cg-Tg(Col1a1-cre/ERT2)1Crm/J (Col2.3-cre)[53], and B6.Cg-Gt(ROSA)26Sortm9(CAG-tdTomato)Hze/J (Rosa26-tdTomato) mice were from Jackson Laboratory[54]. B6.CBA-Tg(Cdh5-cre/ERT2)1Rha was kindly provided by Ralf H. Adams (Max Planck). *Dll4*^{i3COIN} model was provided by Aris Economides[55]. *Dll1*$^{fl/fl}$ animals were previously described[56]. To generate the full-length BAC transgenes, we used C57BL/6 (B6) mouse genomic BAC clone RP23–46P4 (mDll4), RP23–113N21 (mDll1) and RP23–19018 (mJag1) obtained from the Children's Hospital Oakland Research Institute (CHORI) repository and modified by recombination in bacteria as described[57]. The cassette containing mCherry cDNA, polyA signal and FRT-flanked bacterial zeocin resistance gene (ZeoR)[58] was recombined into the first exon, and ZeoR was removed by FLP-mediated recombination. BAC transgenes were digested with NotI and injected into fertilized oocytes of (B6xDBA2)F1 hybrid mice or pure inbred B6 mice.

To induce Cre-mediated gene inactivation, animals were injected with 1,000μg tamoxifen (Sigma, T5648) intraperitoneally every day for 5 days. All mice were rested for 14 days before subjecting them to a second round of 5 tamoxifen injections. Animals were analyzed 1–3 months following tamoxifen injection. Both male and female sex-matched littermate controls were used for all studies. For 5-FU treatments, mice were injected intraperitoneally once with 150mg kg-1 5-FU (Sigma-Aldrich, F6627–5G) or PBS. All 5-FU-injected animals were screened for efficient myeloablation by BM cellularity measurement. All animal experiments were performed in accordance with protocols approved by the New York University Institutional Animal Care and Use Committee.

Flow cytometry.

BM cells were isolated by flushing the long bones in PBS with 2% fetal bovine serum on ice. Single-cell suspensions of thymus and spleen were obtained by gentle tweezing of the organs with forceps. The cells were dissociated to a single-cell suspension by filtering through a 70μm nylon mesh. Nonspecific antibody binding was blocked by incubation with 2.4G2. Cells were incubated with primary antibodies for 60 min and streptavidin conjugates, when applicable, for 15 min on ice.

All antibodies were purchased from BD-Pharmingen or e-Bioscience. We used the following fluorochrome or biotin conjugated antibodies: CD117 (2B8), Sca-1 (D7), CD11b (M1/70), Gr-1 (RB6–8C5), NK1.1 (PK136), TER-119, CD3 (145–2C11), CD127 (A7R34), CD34 (RAM34), FcγRII/III (2.4G2 or 93), CD135 (A2F10.1), CD4 (RM4–5), CD8 (53–6.7), CD150 (9D1), B220 (RA3–6B2), CD48 (HM481). BM lineage antibody cocktail included CD11b, Gr-1, NK1.1, TER-119, CD4, CD8, B220.

For flow cytometric analysis of VEcad-cre;*LoxP*-tdTomato and *Lepr*-cre;*LoxP*-tdTomato, the whole BM (two femurs, two tibias, and two ileums) was flushed and digested with LiberaseTM (0.2 mg/ml)) and DNase I (200U/ml) at 37°C for 60min at 550 rpm shaking with additional mixing the cells every 10 min with pipetting. For flow cytometric analysis of Col2.3-cre;*LoxP*-tdTomato, the animals were first injected with 1,000μg tamoxifen (Sigma, T5648) intraperitoneally three times and were processed two weeks following the last injection. Two weeks following the last injections femurs, tibias, and ileums were isolated, cut into 2mm pieces and digested with LiberaseTM and DNase I at 37°C for 90min at 550 rpm shaking with additional mixing the cells every 10 min. Following digestion, the cells were placed on ice and the reaction was quenched with FACS buffer with 1% 0.5M EDTA (Fisher Bioreagents).

For analysis of BM endothelial cells, mice were i.v. injected with 10ug/mouse eFluor660 conjugated anti-VE-cadherin antibody (BV13, eFluor 660, eBioscience). Fifteen minutes later, the animals were euthanized, the long bones were removed, and BM was flushed, digested and stained as above. Data were analyzed by FACSDiva (BD) or FlowJo (Tree Star) software.

Immunofluorescent Labeling.

Tissues were dissected from euthanized animals and fixed overnight in 4% paraformaldehyde (PFA) at 4°C. For analysis by IF, fixed tissues were placed in 30% sucrose solution for 24 hours and subsequently frozen in OCT. Bones were decalcified in 0.5M EDTA solution (Fisher Scientific) for 6 days at 4°C, placed in 30% sucrose solution for 24 hours at 4°C, and frozen in OCT. BM 6–8 mm cryostat sections were dried at RT overnight in the dark, rehydrated and stained with anti-RFP (1:200) (Abcam) antibody at 4°C overnight. For osteo populations IF, primary antibodies against murine Mmp14 (Abcam, ab78738, 1:100), Cd9 (BosterBio, M01202, 1:50), or Car3 (Abcam, ab118428, 1:100), CD63-APC (NVG2), CD200-APC (0X90) were added and incubated in a wet dark chamber overnight at 4°C. For vascular and perivascular populations the following antibodies were used: Endomucin (Santa Cruz, V.7C7, 1:100), CD31 (R&D, 1:100), Laminin (Abcam,

1:100), Sca-1 (BioLegend, 1:100), Icam2 (BD Pharmingen, 1:100), Podocalyxin (R & D, 1:100), VEGFR3(R & D, 1:100), ICAM1 (BioLegend,1:100), ESM1 (R&D, 1:100), CD200 (Biolegend, 0X90, 1:100), CD63 (Biolegend, NVG2, 1:100). When indicated, the sections were stained with DAPI for 5 min and mounted with Fluoromount-G (Southern Biotech). Images were taken using Leica TCSSP5 II Confocal Microscope and analyzed on Leica Microsystems imaging software.

For, early progenitors ($Lin^{-}CD48^{-}CD150^{+}$) progenitors imaging, *mDll4-mCherry* animals were anesthetized and injected with 25ug BV13 (Biolegend) conjugated to Alexa Fluor 647 (Life Technologies). After 10 minutes, mice were euthanized according to IACUC protocol. Long bones were freshly isolated and decalcified in 10% EDTA for 72 hrs at room temperature. Bones were cryopreserved in 30% Sucrose for 48 hrs at 4°C and then embedded in a 50% O.C.T. (Tissue-Tek) and 50% (30%) Sucrose mixture and placed on a liquid nitrogen bath. Bones were then sectioned on a Leica CM 3050 S cryostat in 12-micron slices and collected on slides using the Leica CryoJane tape-transfer method. Slides were brought to room temperature and immersed in a blocking solution (10% Normal Goat Serum [Jackson Laboratories], 0.1% Triton X-100) for 30 minutes at room temperature, protected from light. Blocking solution was removed and sections were immersed in desired primary conjugated antibody combinations diluted in blocking and incubated overnight at 4°C. The following antibodies were used for staining: Lineage (Ter119 (Biolegend, Ter119, 1:100), CD41 (Biolegend, MWReG30, 1:100), CD11b (Biolegend, M1/70, 1:100), Gr1 (Biolegend, RB6–8C5, 1:100), B220 (Biolegend, RA3– 6B2, 1:100), CD48 (Biolegend, HM48–1, 1:100), CD150 (Biolegend, TC15–12F12.2, 1:100)). Sections were washed and immersed in desired secondary antibodies in blocking solution for 30 minutes at room temperature. Slides were washed and counterstained with DAPI (1:5000, Biolegend) for 10 minutes at room temperature. Slides were washed, mounted with Prolong Gold (Life Technologies) anti-fade solution and cover slipped for imaging. Images were taken on a Nikon C2 confocal laser scanning microscope.

Intravital BM imaging.

Mice were anesthetized using isoflurane and secured on a warming imaging plate in a supine position. The medial or soleus region of the tibia was surgically exposed removing soft tissue. The bone was carefully thinned using a microdrill. Exposed tibia was mounted and immobilized with a metal plate, with an imaging window. All images were collected on an Olympus FV-1000MPE upright laser scanning microscope with a 25X 1.05 NA water immersion objective using a Spectra-physics DeepSee-MaiTai Ti:sapphire pulsed laser for excitation, with emission filters for the detection of second harmonic (compact bone), FITC (GFP), rhodamine (Tomato or DsRed fluorescent proteins) and qdot 705 (Invitrogen). To visualize mCherry expression, Ti-Sapphire laser excitation was tuned to 740nm and emission collected by non-descanned PMT using a 595–645nm filterset.

CFU-F assay.

1×10^3 sorted cells were seeded per well in a 6-well adherent tissue culture plate using phenol red–free alpha-MEM (Gibco) media supplemented with 15% FBS (Gibco), 10% MesenCult stimulatory supplement (STEMCELL Technologies), and 0.5% penicillin-

streptomycin. One half of the media was replaced after 7 days and at day 14 cells were stained with Giemsa staining kit (EMD Chemicals) and colonies counted.

RNA extraction and population-based RNA-seq.

Total RNA was extracted from samples using RNeasy Plus Micro Kit (Life Technologies). Libraries were generated with SMART-Seq® v4 Ultra™ Low Input RNA Kit for Sequencing and Low Input Library Prep Kit v2 (Takara Bio #634899). Libraries were sequenced on an Illumina HiSeq 4000 sequencer. Sequencing results were demultiplexed and converted to FASTQ format using Illumina bcl2fastq software. The sequencing reads were aligned to the mouse genome (mm10/GRCm38) using the splice-aware STAR aligner[59]. The featureCounts program[60] was utilized to generate counts for each gene based on how many aligned reads overlap its exons. These counts were then normalized and used to test for differential expression using negative binomial generalized linear models implemented by the DESeq2 R package[61].

Single-cell library preparation and sequencing.

For scRNA-seq libraries we sorted the following cellular subsets: VEcad-tdT (pooled n=3 animals, 12w), Lepr-tdT (pooled n=2; 12w), and Col2.3-tdT (pooled n=3; 16w); PBS-treated VEcad-tdT (pooled n=5 animals, 6 and 14w), Lepr-tdT (pooled n=2; 18 and 22w), and Col2.3-tdT (pooled n=3; 5 and14w); and 5-FU-treated VEcad-tdT (pooled n=14 animals; 14w), Lepr-tdT (pooled n=4, 18 and 22w), and Col2.3-tdT (pooled n=3; 5 and 14w). For the replicate scRNA-seq experiments the following cellular subsets were sorted: PBS-treated VEcad-tdT (pooled n=3 animals, 9w), Lepr-tdT (pooled n=2; 7w) and 5-FU treated VEcad-tdT (pooled n=4 animals; 9w), Lepr-tdT (pooled n=3, 7w). The libraries were prepared using the Single Cell 3' Reagent Kits v2: Chromium™ Single Cell 3' Library & Gel Bead Kit v2, PN-120237; Single Cell 3' Chip Kit v2 PN-120236 and i7 Multiplex Kit PN-120262" (10x Genomics)[62], and following the Single Cell 3' Reagent Kits v2 User Guide (Manual Part # CG00052 Rev A). Libraries were run on an Illumina HiSeq 4000 as 150 bp paired-end reads, one full lane per sample. We generated eight total libraries for the original set of experiments (Figs. 1–3) and four additional libraries for the validation experiments (Extended Data Fig. 7). In the first set of the experiments three libraries were generated using untreated animals, two libraries were generated using animals treated with PBS, and three libraries were generated upon treatment with 5-FU. For the second set of the experiments two libraries were using animals treated with PBS and libraries were generated upon treatment with 5-FU.

For LSK scRNA-seq libraries, control and *VEc-Dll4*^{i3COIN} animals were treated with tamoxifen to induce *Dll4* deletion as described, and allowed to recover for two weeks. Next, LSKs (Lineage$^-$Sca-1$^+$CD117$^+$) from littermate control (pooled n=2; 10w) and *VEc-Dll4*^{i3COIN} (pooled n=2; 10w) were sorted on FACSAria™ II and libraries prepared as described.

scRNA-Seq data pre-processing.

Sequencing results were demultiplexed and converted to FASTQ format using Illumina bcl2fastq software. The Cell Ranger Single-Cell Software Suite (https://support.

10xgenomics.com/single-cell-gene-expression/software/pipelines/latest/what-is-cell-ranger) was used to perform sample demultiplexing, barcode processing, and single-cell 3' gene counting. The cDNA insert was aligned to the mm10/GRCm38 reference genome. Only confidently mapped, non-PCR duplicates with valid barcodes and UMIs were used to generate the gene-barcode matrix containing 20,097 cells. Further analysis including quality filtering, the identification of highly variable genes, dimensionality reduction, standard unsupervised clustering algorithms, and the discovery of differentially expressed genes was performed using the Seurat R package[63]. To exclude low quality cells, we removed 1,064 cells with fewer than 1,000 detected genes. To exclude cells that were extreme outliers in terms of library complexity and may possibly include multiple cells or doublets, we calculated the of the distribution of genes detected per cell and removing any cells in the top 2% quantile. We also removed cells with more than 10% of the transcripts coming from mitochondrial genes. After quality filtering, the mean and median number of detected genes per cell was 2227.2 and 1999.0, respectively. After removing unwanted cells from the dataset, we normalized the data by the total expression, multiplied by a scale factor of 10,000, and log-transformed the result.

Integrated analysis of single cell datasets.

To account for batch differences, we utilized the Seurat alignment method for data integration[13] which does not expect that confounding variables have uniform effects on all cells in a dataset and allows for global transcriptional shifts between datasets. It uses a variant of canonical correlation analysis (CCA) to find linear combinations of features and identifies shared correlation structures across datasets[13,64,65]. For each dataset, we identified variable genes while controlling for the strong relationship between variability and average expression. We took the union of the top 2,000 genes with the highest dispersion from both datasets and ran CCA to determine the common sources of variation between the two datasets. We then aligned the subspaces based on the first 30 canonical correlation vectors, generating a new dimensional reduction that was used for further analysis.

Visualization and clustering.

To visualize the data, we further reduced the dimensionality of the entire 18,339 cell dataset to project the cells in two-dimensional space using t-distributed Stochastic Neighbor Embedding (tSNE) based on the aligned CCA. Aligned CCA was also used as a basis for partitioning the dataset into clusters using a shared nearest neighbor (SNN) modularity optimization algorithm. Based on the expression levels of the three main population markers *(Cdh5, Lepr, Col1a1),* the three populations formed visually distinct clusters. However, we also noticed small clusters of contaminating cells expressing hematopoietic markers such as *Ptprc* (n=762). These were removed and the clustering process was repeated. As expected, the cells separated into clearly distinct populations corresponding to the expression levels of the three main population markers *(Cdh5, Lepr, Col1a1)* (Fig. 1b, Extended Data Fig. 1e). Using graph-based clustering, we divided the cells into 17 transcriptionally-similar subpopulations. We merged clusters with less than 50 steady state cells with the most biologically similar clusters and removed two small clusters that could not be merged based on biological identity, but were composed of too few cells to represent a real sub-population. The resulting 17,374 cells were divided into 11 clusters (Fig. 3b). We then separated steady

state (n=9,622) and 5-FU treated cells (n=7,752) (Fig. 3a) to initially examine the transcriptional profile at steady state and then in the context of 5-FU treatment.

Determining cluster markers.

To find markers that define individual clusters, we performed pair-wise differential expression analysis using the Model-based Analysis of Single-cell Transcriptomics (MAST) method[66], adjusting for cellular detection rate, for each cluster against all other clusters for autosomal genes detected in at least 20% of the cluster cells, keeping the genes that were significant in each of the comparisons. To visualize how well the resulting gene signatures define the clusters, we randomly subsampled 100 cells from each cluster to neutralize size differences and used the 10 most significant positive markers for heatmap visualization (Fig. 1c), highlighting the variation between sub-clusters within the three major BM niche populations. To reduce the effects of distant niche elements, we additionally recalculated cluster markers relative to only other clusters of the same population (Fig. 2 a–c).

To determine differentially expressed genes in response to 5-FU treatment, we used the genes detected in at least 10% of either group and fold change difference of at least 10%. Significance was determined using the MAST method with Bonferroni multiple-comparison correction.

Independent analysis of single cell datasets.

We repeated the analysis of the VEcad$^+$, LepR$^+$, and Col2.3$^+$ steady state subsets separately. After quality filtering, we retained 10,339 steady state cells. The mean and median number of detected genes per cell were 1884.9 and 1680.0, respectively. We further reduced the dimensionality of the steady state cell dataset and the first 40 principal components were used to partition the dataset into sufficiently distinct 15 clusters. Contaminating hematopoietic cells (n=607) were identified based on the expression of markers such as *Ptprc* and removed. The three populations formed visually distinct clusters and the mixed library was assigned to the appropriate subset based on the expression levels of the population markers *(Cdh5* and *Lepr).* The purified populations were then separated for independent analysis. To account for batch differences when combining the untreated and PBS-treated experiments, we again utilized the Seurat CCA-based alignment method. We aligned the subspaces based on the first 10 canonical correlation vectors VEcad$^+$ and LepR$^+$ subsets and 15 for Col2.3$^+$. We then applied the same approach as in the integrated analysis for determining subpopulations and defining cluster markers. The VEcad$^+$ cells were divided into three clusters (Extended Data Fig. 2b). The initial analysis LepR$^+$ cells based on six clusters revealed a small cluster of VEcad$^+$ cells (n=99) which was removed. Three of the remaining clusters were merged due to their transcriptional similarity (Extended Data Fig. 2e). The Col2.3$^+$ cells were divided into six clusters (Extended Data Fig. 2h).

Validation of 5-FU treatment in single cell datasets.

Additional VEcad$^+$ and LepR$^+$ PBS/5-FU treated scRNA-seq libraries were processed following the same protocol as the original experiment. After quality filtering, we retained 18,747 cells. The mean and median number of detected genes per cell were 2390.7 and 2217.0, respectively. We further reduced the dimensionality of the steady state cell dataset

and the first 40 principal components were used to partition the dataset into 10 clusters. Contaminating hematopoietic cells (n=475) were identified based on the expression of markers such as *Ptprc* and removed. The cells were then summarized based on the four known populations (Extended Data Fig. 7).

LSK scRNA-seq.

To exclude low quality cells and possible multiplets, we calculated the distribution of the numbers of genes detected per cell and removed any cells in the top and bottom 2% quantiles. We additionally removed cells with more than 10% of the transcripts coming from mitochondrial genes. After filtering, the mean and median number of detected genes per cell was 2353.5 and 2231, respectively. We normalized the data by the total expression, multiplied this by a scale factor of 10,000, and log-transformed the result. To account for batch differences, we utilized the Seurat CCA-based alignment method. For each dataset, we took the union of the top 1,000 genes with the highest dispersion from both datasets and ran a CCA to determine the common sources of variation between the two datasets. We then aligned the subspaces based on the first 25 canonical correlation vectors, generating a new dimensional reduction that was used for further analysis. Aligned CCA was used as a basis for tSNE visualization and partitioning the dataset into clusters. To visualize the data, we further reduced the dimensionality of the entire 22,022 cell dataset to project the cells in two-dimensional space using tSNE based on the aligned CCA. Based on the initial clustering, we were able to identify small populations of contaminating cells expressing established lineage markers *(Vpreb1, Ccl5, Ltf, Pf4, Cd74* and *Carl)*[47] (n=906). These were removed and the tSNE was recalculated for the remaining 21,116 cells (Fig. 5d).

Signature-based cell classification.

To classify the cells, we used previously identified gene signatures for HSPC compartments[46]. Population-specific signatures were defined by top 100 genes ranked by the Significance Analysis of Microarrays (SAM) scores. We calculated a module score for each cell based on the average expression levels of every gene signature, subtracted by the aggregated expression of randomly selected control genes[67]. Each cell was assigned to the population with the highest positive score (Fig. 5e). The same scoring approach was used to quantify lineage-specific skewing (Extended Data Fig. 9k, l) and MSC enrichment (Extended Data Fig. 4d). To confirm the identified HSPC subsets, we performed pair-wise differential expression analysis using the MAST method to determine the population-specific markers.

Reconstructing cell development trajectories.

To infer the developmental progression of cells across multiple developmental stages and order them in pseudotime, we used the algorithms implemented in the Monocle package[68]. We subset the dataset to only the 4,883 P1, P2, P3, P4, O1, O2, O3 cells for the analysis. We then identified genes that differ between the clusters based on a likelihood ratio test between a generalized linear model that knows the cell clusters and a model that doesn't. We then selected the top 1,000 significantly differentially expressed genes as the ordering genes for the trajectory reconstruction using the nonlinear reconstruction algorithm DDRTree (Fig. 2d).

Pathway enrichment analysis.

Statistical analysis and visualization of gene sets were performed using the clusterProfiler R package[69] for the genes that were calculated to be cluster markers for the cycling cluster (C) (Extended Data Fig. 5f). Enrichr[70] and WikiPathways cell signaling pathways database were used to determine the enrichment of biological processes based on the genes that were significant upregulated in response to 5-FU treatment in the $LepR^+$ population (Extended Data Fig. 6f).

qRT-PCR.

Total RNA was extracted from samples using RNeasy Plus Micro Kit (Life Technologies) and cDNA was prepared using the High-Capacity RNA-to-DNA Kit (Applied Biosystems). Real time PCR reactions were carried out using TaqMan Gene Expression Master Mix (Life Technologies) and run on a Lightcycler 480 II (Roche). The following genes were analysed with TaqMan Gene Expression Assays: *Gapdh* (Mm99999915_g1), *Dll4* (Mm00444619), *Dll1* (Mm01279269_m1), *Jag1* (Mm00496902_m1), *Cdh5* (Mm00486938_m1), *Lepr* (Mm00440181_m1), *Col1a1* (Mm00801666_g1).

Statistical Analysis.

Statistical analysis (excluding RNA-seq experiments) was conducted using the PRISM program (GraphPad). Two groups were compared using an unpaired t test. To assess the statistical significance of differences between more than two treatments, we used two-way ANOVA. Significance was defined as $*p < 0.05$, $**p < 0.01$, $*** p < 0.001$.

Data availability

The raw sequencing data and expression-count data are deposited in GEO, accession number GSE108892. An interactive query and visualization tool for different BM niche populations is also available at http://aifantislab.com/niche. Online Content Methods, along with any additional Extended Data display items and Source Data, are available in the online version of the paper; references unique to these sections appear only in the online paper.

Extended Data

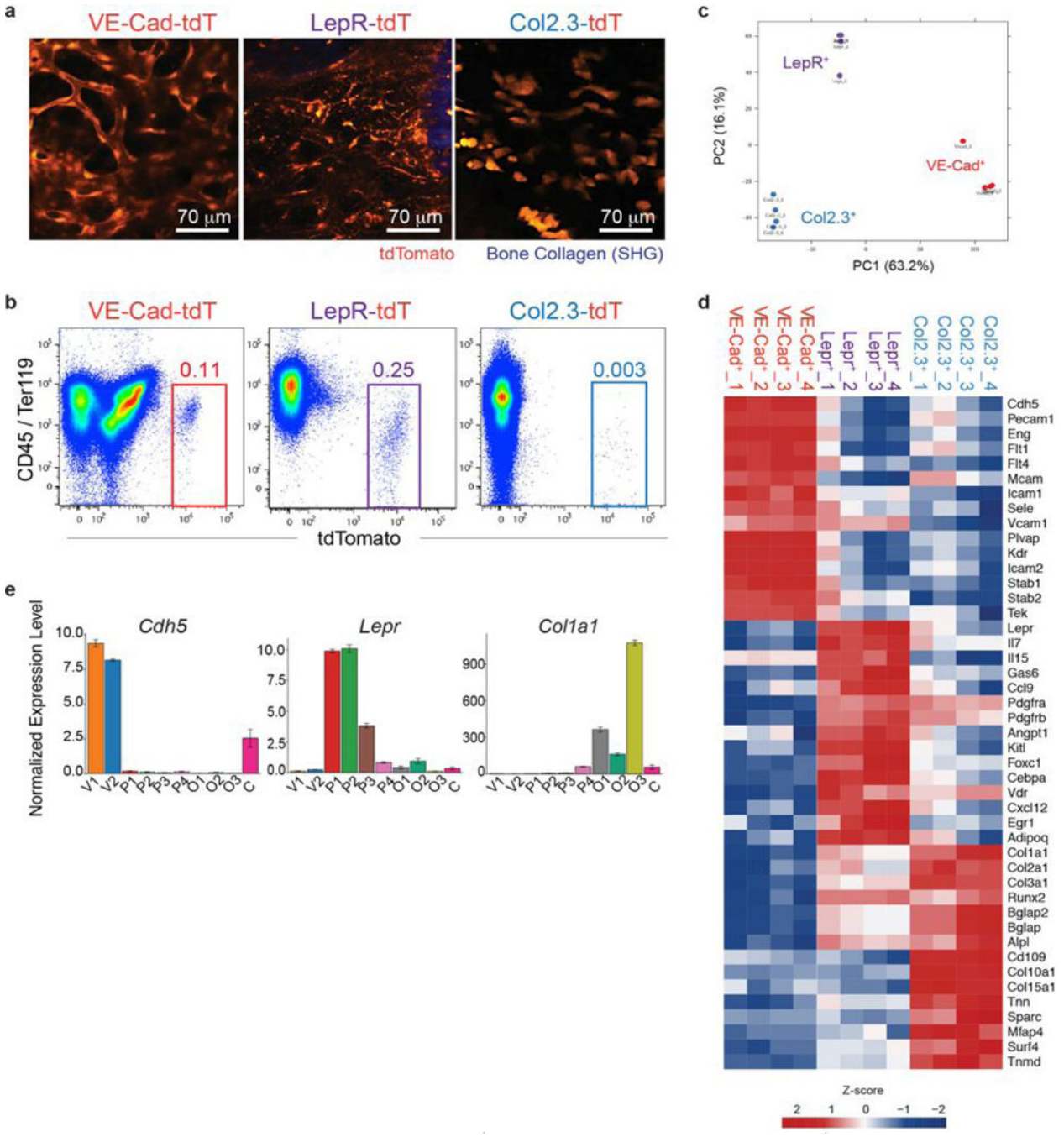

Extended Data Figure 1:

RNA-seq analysis of the bone marrow microenvironment populations.

a, Representative two-photon imaging of tdTomato$^+$ vascular cells (VE-Cad—tdTomato$^+$), perivascular cells (LEPR—tdTomato$^+$) and osteoblasts (COL2.3—tdTomato$^+$). **b**, Representative flow cytometry of VE-Cad-tdTomato$^+$, LEPR-tdTomato$^+$ and COL2.3-tdTomato$^+$ populations. **c**, Principal component analysis of vascular (VE-Cad-tdTomato$^+$, n = 4) (red), perivascular LEPR$^+$ (LEPR-tdTomato$^+$, n = 4) (purple) and osteoblast (COL2.3-tdTomato$^+$, n = 4) (blue) populations, based on the expression of the 1,000 most-variable

genes in bulk RNA-seq. **d**, Relative expression levels of COL2.3^{+}, LEPR^{+}and VE-Cad^{+} signature genes across the three subpopulations of the bone marrow niche in bulk RNA-seq. Normalization and statistical analysis were performed using the DESeq2 R package. **e**, Normalized expression levels of the population-specific markers VE-Cad (*Cdh5*), LEPR (*Lepr*) and COL2.3 (*Col1a1*) for all scRNA-seq clusters. n = 9,622 cells. The data are mean ± s.e.m. Experiments were repeated independently on more than 10 (**a, b**) biological samples with similar results.

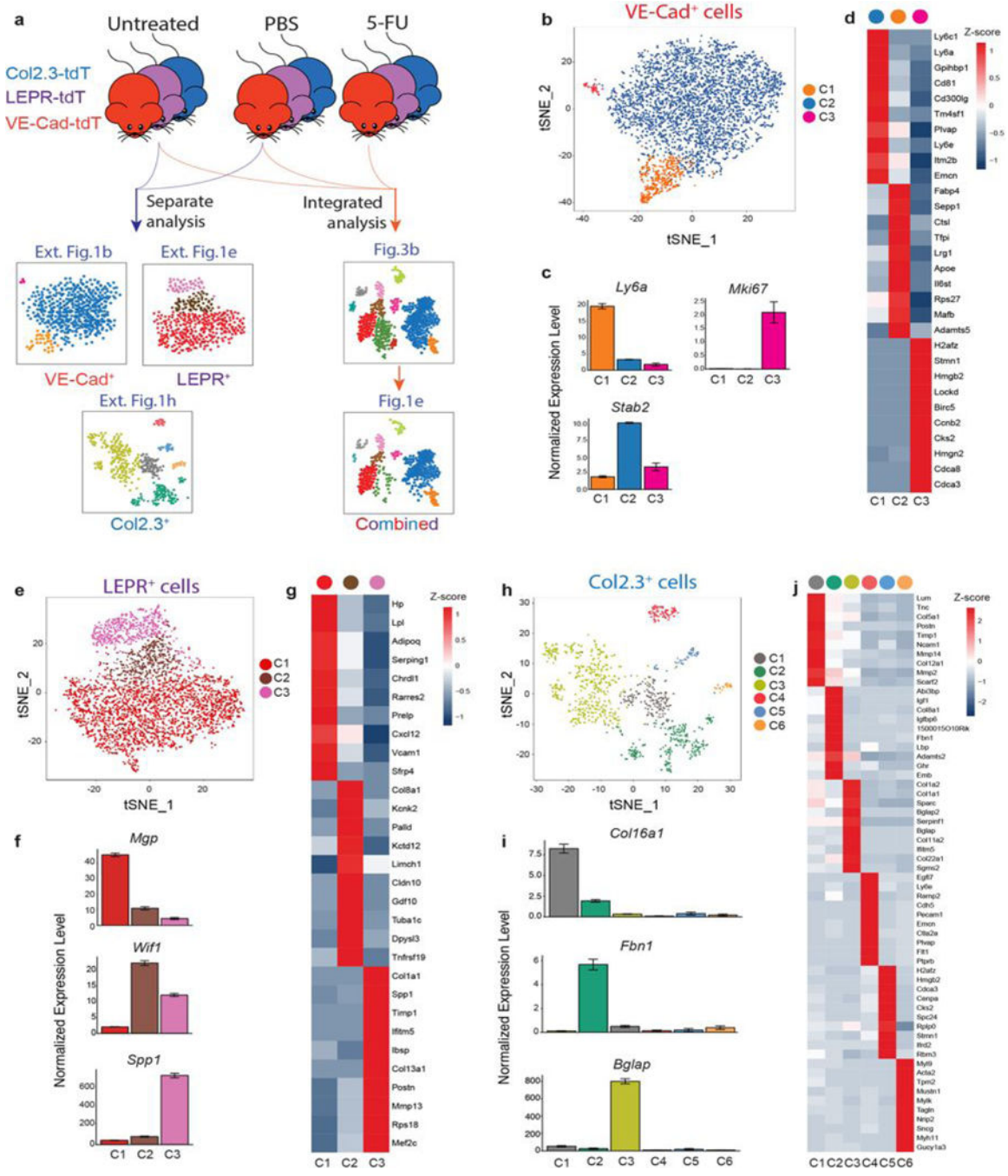

Extended Data Figure 2:

Analysis of VE-Cad$^+$, LEPR$^+$ and COL2.3$^+$populations.

a, Schematic workflow of independent and integrated analysis of VE-Cad$^+$, LEPR$^+$ and COL2.3$^+$ scRNA-seq data. **b**, *t*-SNE representation of VE-Cad$^+$ populations only. Cluster C1 corresponds to arterial cluster V1 (*Ly6a*^{high}). Cluster C2 corresponds to sinusoidal cluster V2 (*Stab2*^{high}). Cluster C3 is the cycling cluster. **c**, Normalized expression of arterial, sinusoidal and cycling markers (*Ly6a, Stab2* and *Mki67*, respectively) (n = 4,551 cells). **d**, Gene signatures of VE-Cad$^+$subpopulations in the bone marrow, based on the relative

expression levels of the ten most-significant markers for each cluster. **e**, *t*-SNE representation of the LEPR$^+$ population only. Cluster C1 corresponds to the adipocytic-primed cluster P1 (*Mgp*^{high}) and encompasses cluster P2. Cluster C2 corresponds to P3 (*Wif1*^{high}), and C3 to P4 (*Spp1*^{high}). **f**, Normalized expression of P1, P3 and P4 markers (*Mgp, Wif1* and *Spp1*, respectively). *n* = 3,907 cells. **g**, Gene signatures of LEPR$^+$subpopulations in the bone marrow, based on the relative expression levels of the ten most-significant markers for each cluster. **h**, *t*-SNE representation of the COL2.3$^+$ population only. Cluster C1 corresponds to cluster O1 (*Col16a1*^{high}), cluster C2 to O2 (*Fbn1*^{high}) and C3 to O3 (*Bglap*^{high}). **i**, Normalized expression of O1, O2 and O3 markers (*Col16a1, Fbn1* and *Bglap*, respectively). *n* = 1,114 cells. **j**, Gene signatures of COL2.3$^+$ subpopulations in the bone marrow, based on the relative expression levels of the ten most-significant markers for each cluster. Cluster C4 represents arterial vascular cells (*Cdh5, Kdr* and *Ly6e*); C5 is glial-like cells (*Fabp7, Mpz* and *Endrb*); and C6 is myocyte-like cells (*Pgf, Pln* and *Acta2*). The data shown in **c, f, i** are mean ± s.e.m. MAST with Bonferroni correction (**d, g, j**).

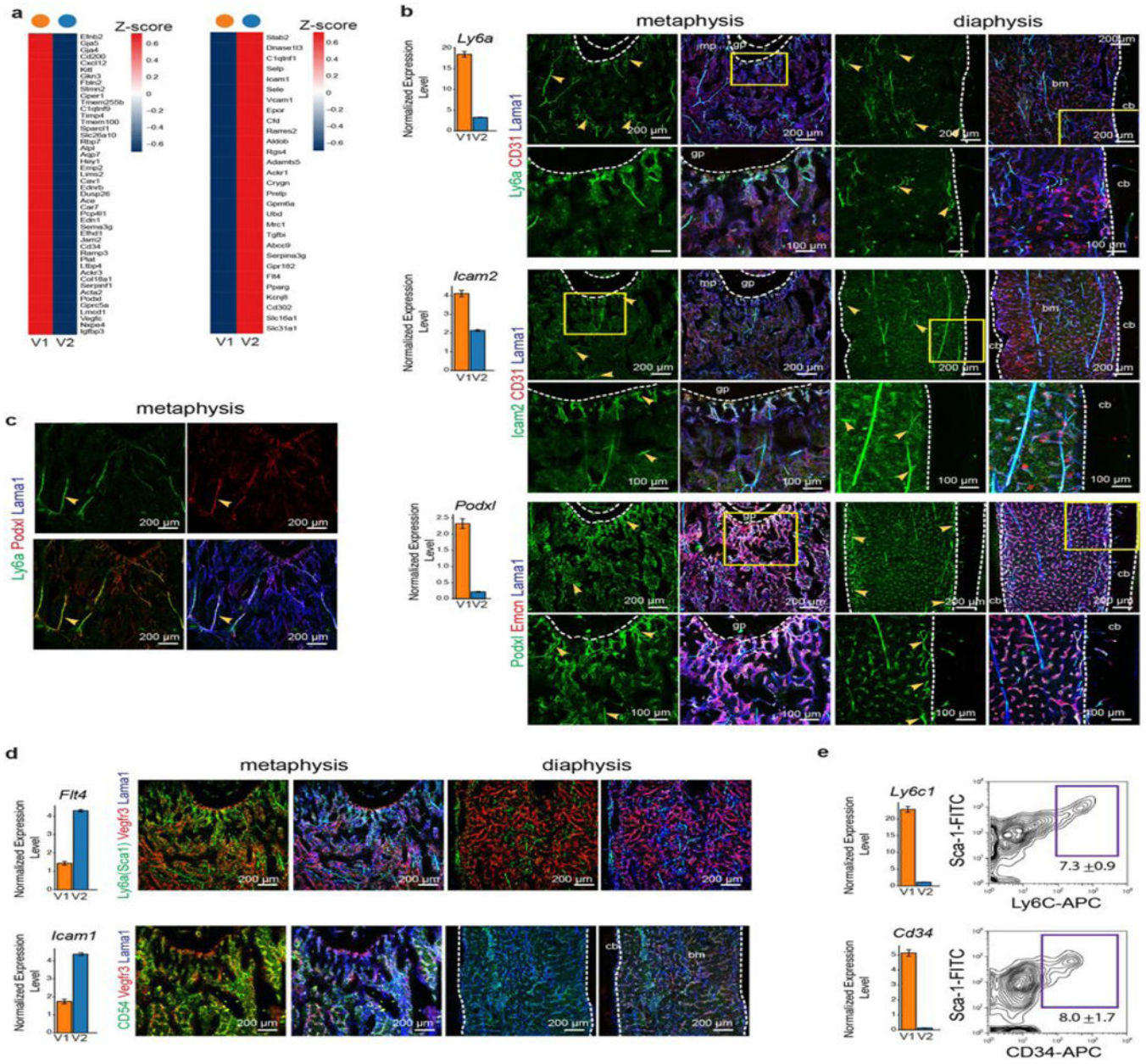

Extended Data Figure 3:

Characterization of VE-Cad^{+} subpopulations.

a, Relative average scRNA-seq expression levels of the previously described arterial and sinusoidal gene signatures at a steady state, within the VE-Cad^{+} clusters V1 and V2. **b**, Average scRNA-seq expression levels (left) (n = 4,669 cells) and bone marrow immunofluorescence (right) of arterial expression of SCA-1 (*Ly6a*), CD102 (*Icam2*) and PODXL (*Podxl*) (n = 3 mice); LAMA1 staining (blue) labels all bone vessels; yellow arrowheads indicate arterial vessels. Dashed lines mark bone marrow (bm), compact bone (cb), growth plate (gp) and metaphyseal (mp) bone regions. **c**, Bone marrow immunofluorescence of arterioles co-stained with SCA-1 and PODXL. n = 3 mice. **d**, Average scRNA-seq expression levels (left) and bone marrow immunofluorescence (right) of

sinusoidal VEGFR3 (*Flt4*) (red) and CD54 (*Icam1*) (green) markers. $n = 3$ mice. LAMA1 staining (blue) labels all bone vessels. **e**, Average scRNA-seq expression levels and representative flow cytometry analysis of the arterial subpopulation (V1) using SCA-1 and scRNA-seq-identified LY6C (*Ly6c1*) and CD34 (*Cd34*) from VE-Cad–tdTomato bone marrow ($n = 3$ mice). Cells were pre-gated on DAPI^{-}tdTomato^{high} cells. The data in **b, d**, eare mean ± s.e.m.

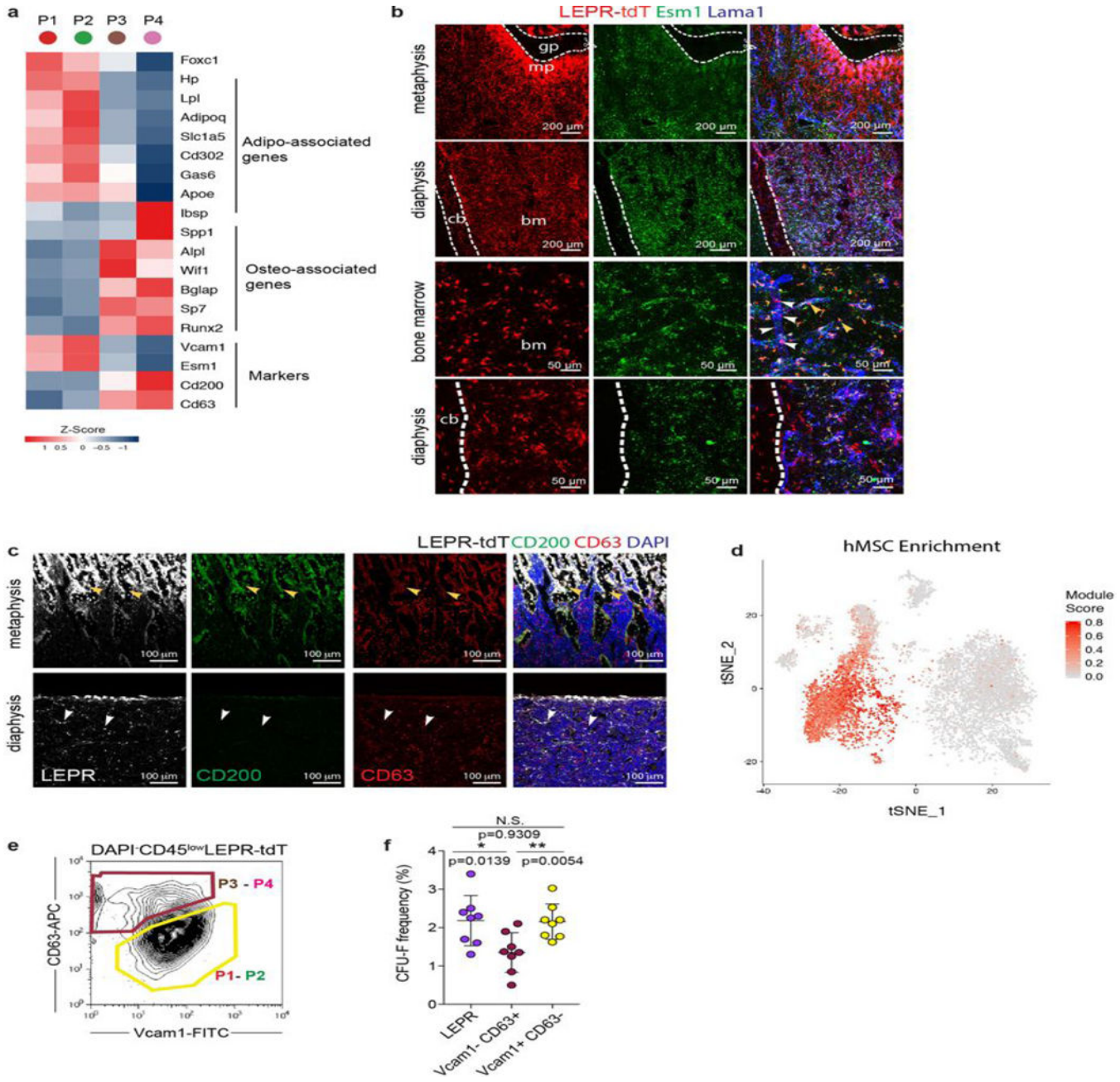

Extended Data Figure 4:

Characterization of perivascular LepR$^+$ subpopulations.

a, Relative average scRNA-seq expression levels of the adipocytic(*Hp, Lpl, Adipoq, Slc1a5, Cd302, Gas6* and *Apoe*) and osteo-associated (*Ibsp, Spp1, Alpl, Wif1, Bglap, Sp7* and *Runx2*)genes, as well as markers used for characterization of LEPR$^+$ cell (*Esm1, Vcam1, Cd200* and *Cd63*). **b**, ESM1 (green) bone marrow immunofluorescence of LEPR-tdTomato femur. LAMA1 staining (blue) labels all bone vessels. Yellow arrowhead, LEPR$^+$ESM1$^+$ cells; white arrowheads indicate LEPR$^+$ESM1$^-$ cells. **c**, CD200 (green) and CD63 (red) bone marrow immunofluorescence of LEPR-tdTomato femur. Nuclei, DAPI (blue). Yellow arrowhead, LEPR$^+$, CD200$^+$, CD63$^+$ cells; white arrowhead, LEPR$^+$, CD200$^-$, CD63$^-$ cells.

d Human mesenchymal stem cell (hMSC) gene signature module score, overlaid on *t*-SNE representation (n=9,622 cells). **e**, Flow cytometry representation of $VCAM1^{high}CD63^{low}$ and $VCAM1^{low}Cd63^{high}$ cells of $tdTomato^{+}$ subpopulations in LEPR-tdT bone marrow. Cells were pre-gated on $DAPI^{-}$ $tdTomato^{high}$ cells. **f**, Fibroblastic colony-forming unit activity of sorted total $LEPR^{+}$ (purple), $LEPR^{+}VCAM1^{low}CD63^{high}$ (maroon), and $LEPR^{+}VCAM1^{high}CD63^{low}$ (yellow) cells from bone marrow of LEPR-tdTomato mice (n=8).The data are mean ± s.d. (**f**). N.S., not significant, $*P \leq 0.05$, $**P \leq 0.01$, $***P \leq 0.001$ (Student' *t*-test, two-tailed (**f**). Data are representative of two (**b, c**) or three (**e, f**) independent experiments.

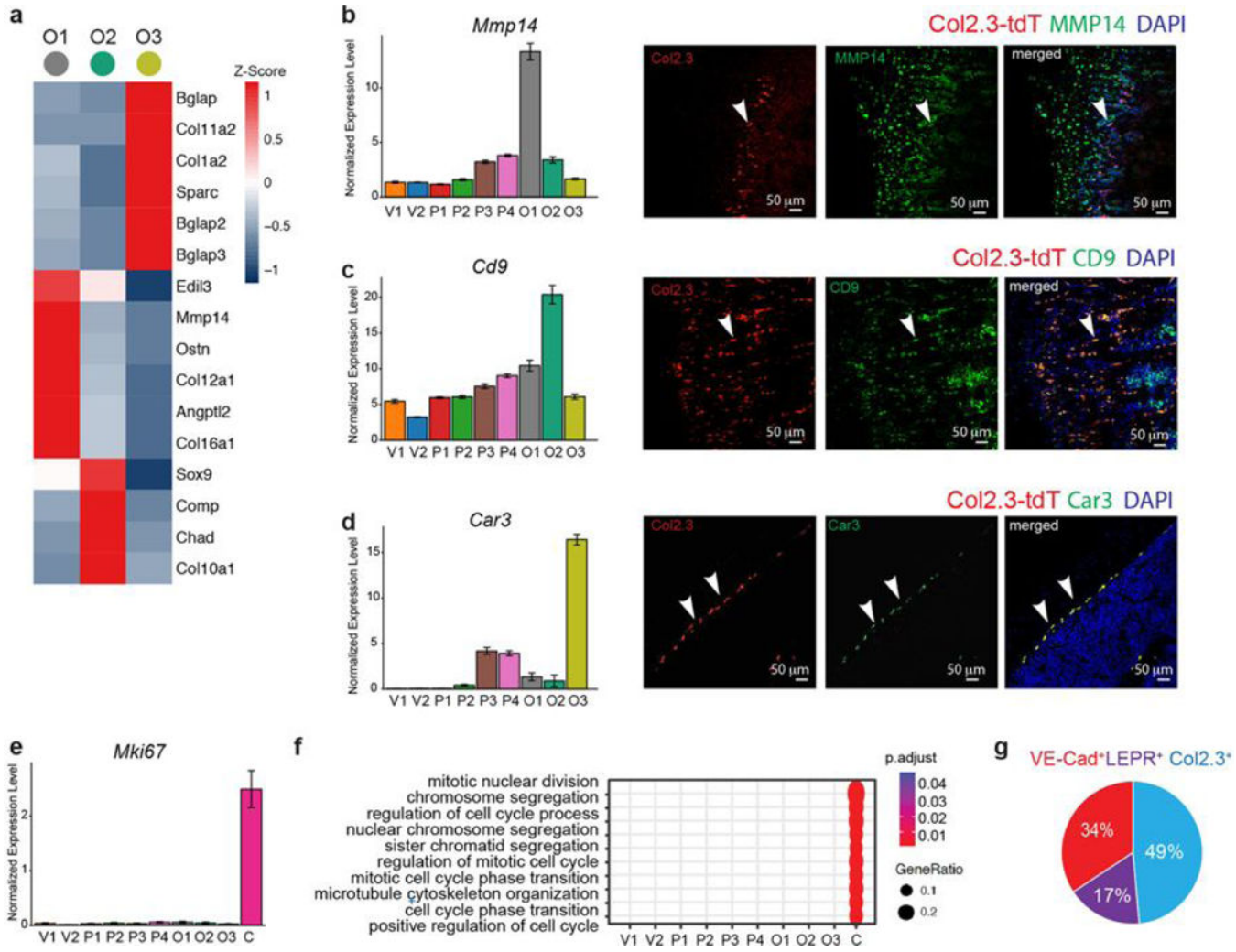

Extended Data Figure 5:

Characterization of Col2.3^{+} subpopulations and cycling cells.

a, Relative average scRNA-seq expression levels of O1 (*Edil3, Mmp14, Ostn, Col121, Angptl2* and *Col16a1*), O2- (*Sox9, Comp, Chad* and *Col10a1*), and O3- (*Col11a2, Col1a2, Sparc, Bglap2* and *Bglap3*) associated genes. **b-d**, Average scRNA-seq expression levels (n = 9,622 cells) and bone marrow immunofluorescence of MMP14 (green) (**b**) (n = 3 mice), CD9 (green) (**c**) (n = 3 mice) and CAR3 (green) (**d**) (n = 3 mice) in Col2.3-tdTomato femur, with arrows indicating co-staining with tdTomato (red). Nuclei, DAPI (blue). Arrowhead, Col2.3^{+}MMP14^{+} (**b**), COL2.3^{+}CD9^{+} (**c**), and COL2.3^{+}CAR3^{+} (**d**). **e**, Expression levels of *Mki67* in all identified subpopulations (n = 9,622 cells). **f**, Enriched Gene ontology biological processes terms most-strongly associated with cycling cluster (C), color-coded by significance of enrichment and size on the basis of the fraction of overlapping genes. n = 9,622 cells. **g**, Contribution of VE-cad-tdTomato^{+}, LEPR-tdTomato^{+}, and COL2.3-tdTomato $^{+}$ cells to the cycling cluster (C) at steady state n = 70 cells. The data **b-e** are mean ± s.e.m

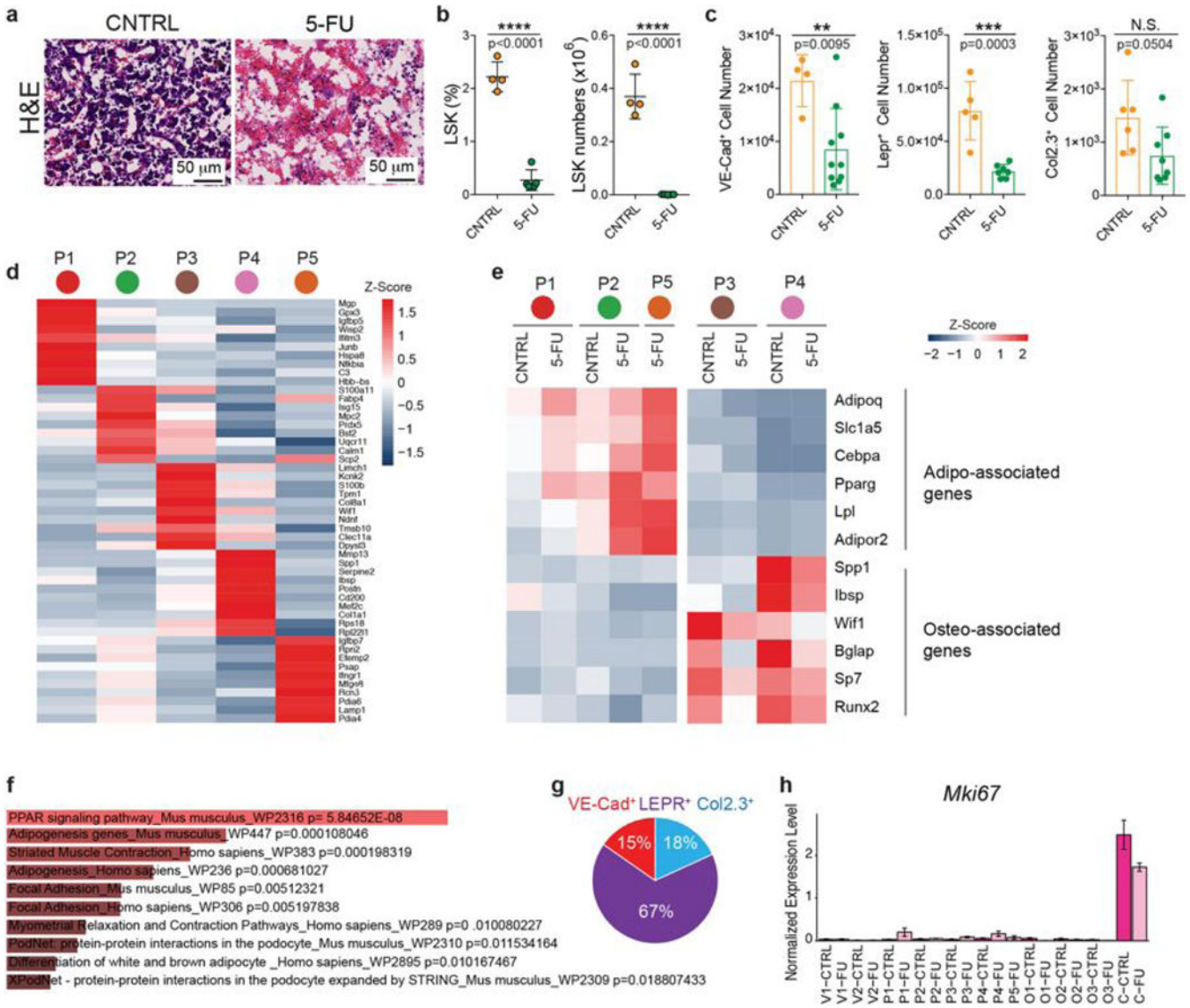

Extended Data Figure 6:

Effect of treatment with 5-FU on subsets of the bone marrow niche.

a, Representative hematoxylin and eosin-stained sections of BM on day 5 following control or 5-FU treatment ($n = 3$ animals). **b**, Frequency and numbers of BM LSK cells on day 5 following control (CNTRL) ($n = 4$) or 5-FU treatment ($n = 5$). **c**, Absolute numbers of BM niche cells, vascular VEcad$^+$ (CNTRL: $n = 4$; 5-FU: $n = 10$), perivascular LepR$^+$ (CNTRL: $n = 2$; 5-FU: $n = 5$), and Col2.3$^+$ osteoblasts (CNTRL: $n = 4$; 5-FU: $n = 5$) from control (PBS) and 5-FU treated animals. **d**, Gene signatures of niche LepR$^+$ sub-populations, including cluster P5, based on the average relative expression levels of the 10 most significant markers for each cluster exclusively within the LepR$^+$ subset. MAST with Bonferroni correction. **e**, Relative expression levels of upregulated adipogenesis-associated genes and downregulated osteogenesis-associated genes in LepR$^+$ subpopulations in response to 5-FU treatment. **f**, LepR$^+$ cells enriched pathways in response to 5-FU treatment ($n = 17,374$ cells). Fisher exact test. **g**, Contribution of VEcad-tdT$^+$, Lepr-tdT$^+$, and Col2.3-tdT$^+$ cells to cycling

cluster (C) following 5-FU treatment (n = 418 cells). **h**, Expression levels of *Mki67* in all identified subpopulations at steady state and following 5-FU (n = 17,374 cells). Data are mean ± s.d. *$P \leq 0.05$, **$P \leq 0.01$, ***$P \leq 0.001$ (Student's t-test, two-tailed) (**b-c**). The data (**h**) are mean ± standard error.

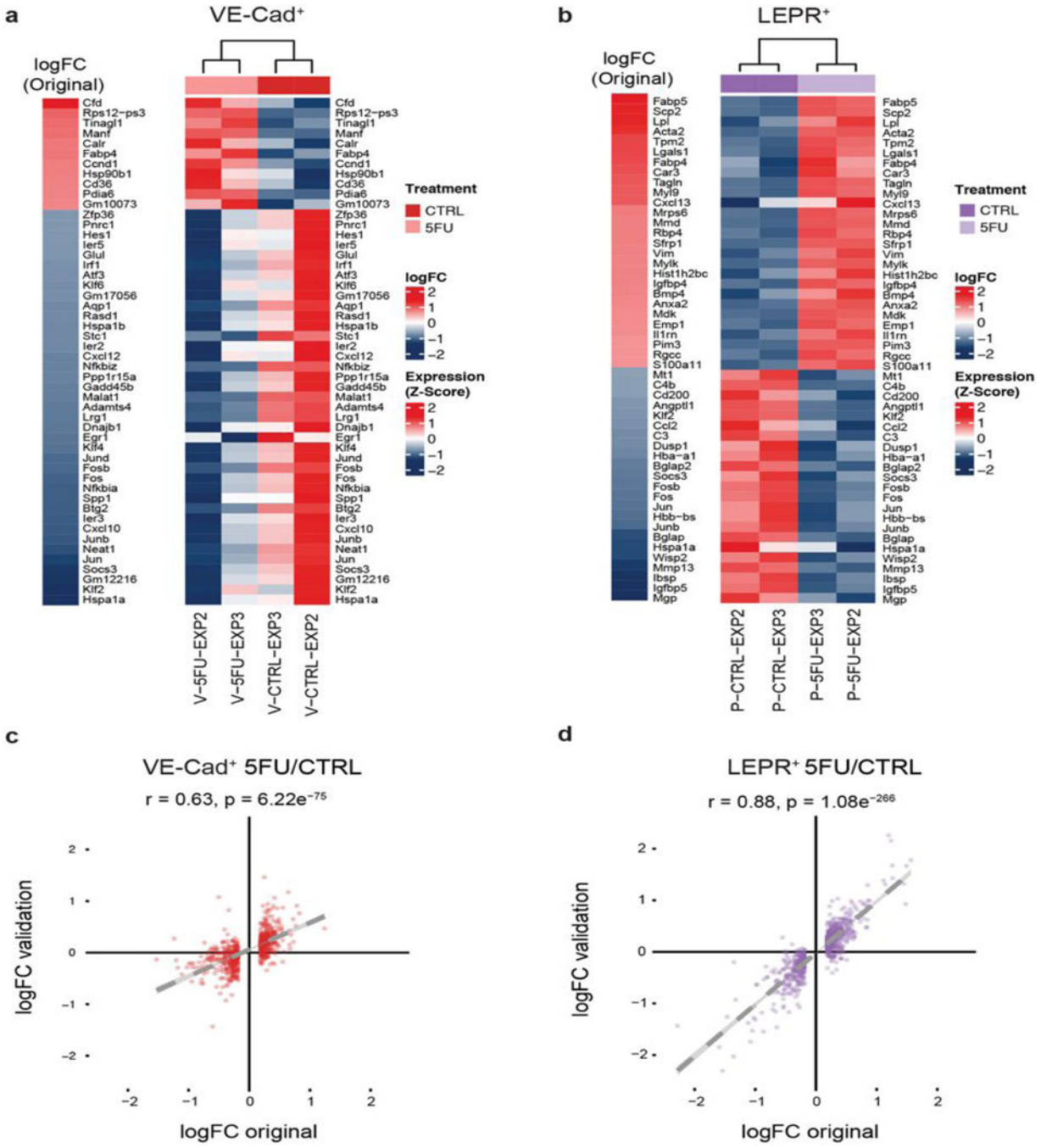

Extended Data Figure 7: Validation of scRNA-seq in VE-Cad$^+$ and LEPR$^+$cells following treatment.

a, b, Heat map and hierarchical clustering of mean normalized expression values of VE-Cad $^+$ (**a**) and LEPR$^+$ (**b**) control-treated and 5-FU-treated samples for 5-FU-modulated genes (top 50 differentially expressed) in two independent scRNA-seq experiments. **c, d**, log-transformed fold changes of differentially expressed genes (up- and downregulated > 1.2×, adjusted *P* value < 0.001) in 5-FU-treated versus control-treated VE-Cad$^+$ (n = 697 genes) cells (**c**) and LEPR$^+$ (n = 829 genes) cells (**d**), for two independent experiments. The trend

line (dashed) and the confidence interval (grey shading) were calculated using the linear model. MAST with Bonferroni correction. VE-Cad$^+$ control-treated, n = 5,796 cells; VE-Cad$^+$ 5-FU-treated, n = 1,481 cells; LEPR$^+$ control-treated, n = 6,128 cells; LEPR$^+$ 5-FU-treated, n = 4,867 cells.

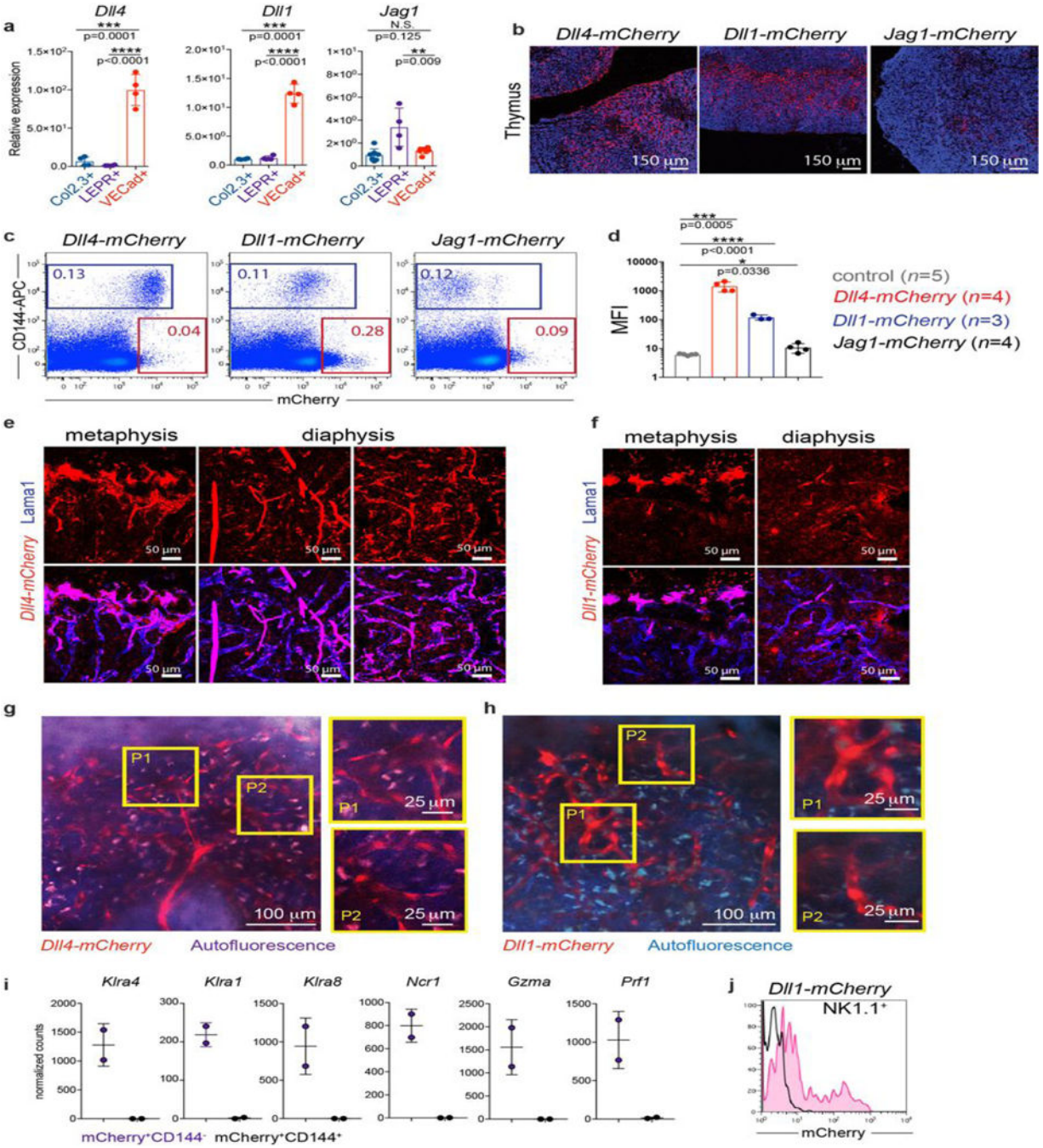

Extended Data Figure 8: Analysis of *Dll4-mCherry, Dll1-mCherry,* and *Jag1-mCherry* reporter animals.

a, Reverse-transcription PCR of *Dll4, Dll1* and *Jag1* in vascular cells (red), perivascular LEPR$^+$ cells (purple) and osteoblasts (blue), normalized to *Gapdh* (n = 4 mice). **b**, Low-magnification immunofluorescence images of thymus sections from *Dll4-mCherry, Dll1-mCherry* and *Jag1-mCherry* mice. **c**, Representative flow cytometry, measuring mCherry fluorescence in total bone marrow of *Dll4-mCherry, Dll1-mCherry* and *JAG1-mCherry* mice. Indicated values represent percentages of the complete CD144$^+$ and mCherry$^+$CD144$^-$

populations. Cells were pre-gated on DAPI^{-} cells. **d**, Representative mCherry levels in DAPI^{-}CD45^{low}TER119^{low}CD144^{+} bone marrow endothelial cells from *Dll4-mCherry* (red) (n = 4), *Dll1-mCherry*(blue) (n = 3), *Jag1-mCherry* (black) (n = 4) and control (grey) (n = 5) mice. **e, f**, Representative immunofluorescence metaphysis and diaphysis of *Dll4-mCherry* (**e**) and *Dll1-mCherry* (**f**) bone marrow (n = 3 mice). mCherry (red) and LAMA1 (blue). **g, h**, Representative two-photon images of bone marrow from intact (left) or dextran-injected (right) *Dll4-mCherry*(**g**) and *Dll1-mCherry* (**h**) mice (n = 3 mice). **i**, Normalized counts of key differentially expressed genes from bulk RNA-seq performed on CD144^{-}DLL1^{+} cells (purple) (from n = 2 mice) and CD144^{+}DLL1^{+} cells (black) (from n = 2 mice). **j**, Representative flow cytometry histogram measuring mCherry fluorescence in NK1.1^{+} population from *Dll1-mCherry* (pink) and control (black) mice (n = 3 mice). The data are mean ± s.d. N.S., not significant, *$P \leq 0.05$, **$P \leq 0.01$, ***$P \leq 0.001$, Student's t-test, two-tailed. Data are representative of two (**a, e–h, j**) or three (**b–d**) independent experiments.

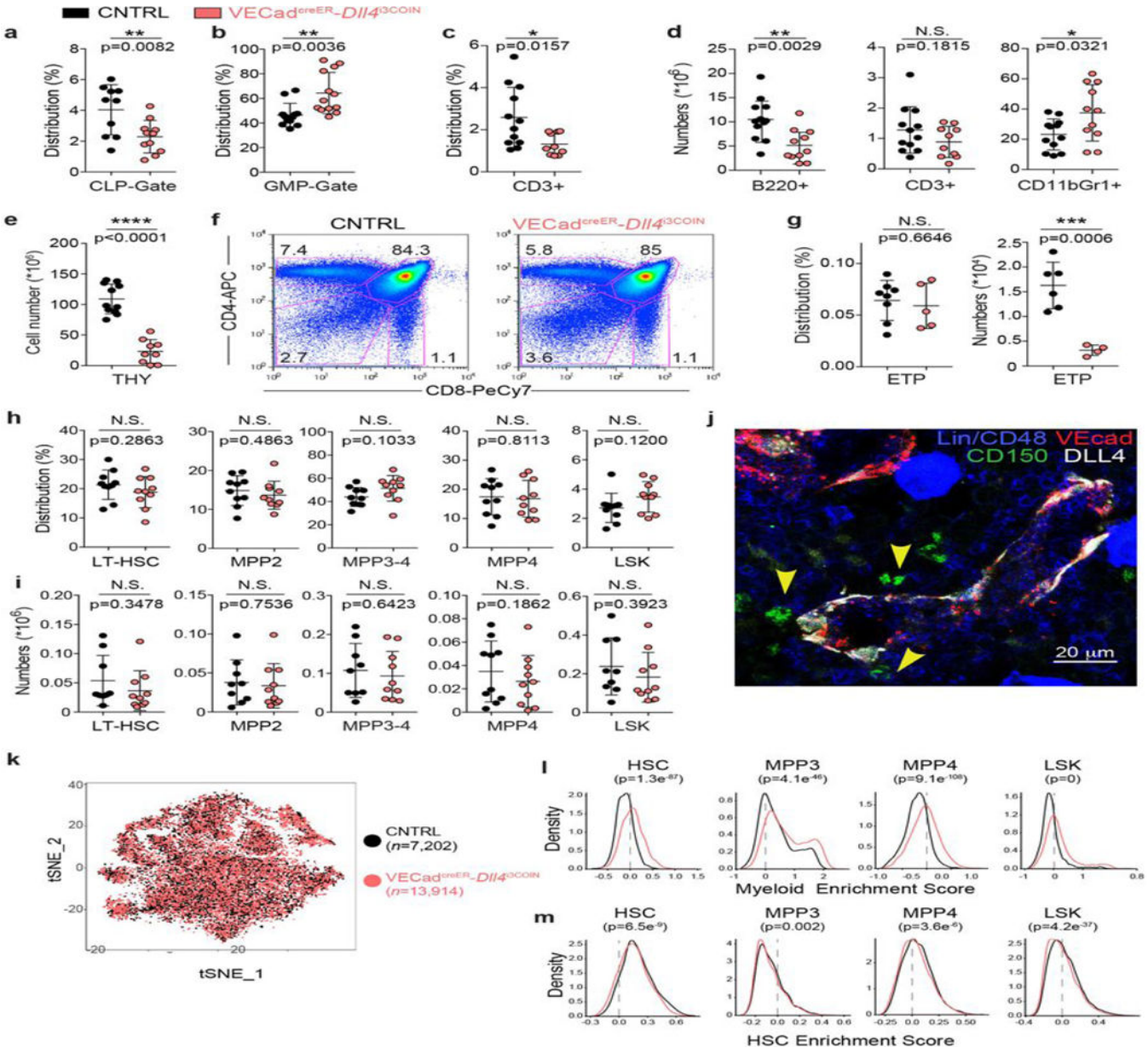

Extended Data Figure 9: Gene expression program of myeloid differentiation is enhanced in VE-Cad-*Dll4*^{i3COIN} HSPCs.

a, b, Representative percentage of bone marrow progenitors in VE-Cad^{creER}-*Dll4*^{i3COIN} and littermate-control mice for common lymphoid progenitors gate (CLP gate) (control, $n = 10$; VE-Cad^{creER}-*Dll4*^{i3COIN}, $n = 11$) (a) and granulocyte–monocyte progenitors gate (GMP gate) (control, $n = 10$; VE-Cad^{creER}-*Dll4*^{i3COIN}, $n = 13$) (**b**). **c**, Frequencies of CD3$^+$ T cells (control, $n = 12$; VE-Cad^{creER}-*Dll4*^{i3COIN}, $n = 11$). **d**, Total numbers of mature haematopoietic subsets in tamoxifen-treated VE-Cad^{creER}-*Dll4*^{i3COIN} and littermate-control mice, including B220$^+$ B cells (control, $n = 10$; VE-Cad^{creER}-*Dll4*^{i3COIN}, $n = 10$), CD3$^+$ T cells (control, $n = 10$; VE-Cad^{creER}-*Dll4*^{i3COIN}, $n = 10$) and CD11b$^+$GR1$^+$ myeloid cells (control, $n = 10$; VE-Cad^{creER}-*Dll4*^{i3COIN}, $n = 10$). **e**, Absolute numbers of thymocytes from VE-Cad^{creER}-*Dll4*^{i3COIN} mice ($n = 11$) and littermate-control mice ($n = 9$). **f**, Representative

flow cytometry analysis of thymic subsets in tamoxifen-treated VE-Cad^{creER}-*Dll4*^{i3COIN} and littermate-control mice. **g**, Frequencies (control, $n = 8$; VE-Cad^{creER}-*Dll4*^{i3COIN}, $n = 5$) and absolute numbers (control, $n = 6$; VE-Cad^{creER}-*Dll4*^{i3COIN}, $n = 4$) of early thymic progenitors in thymi from VE-Cad^{creER}-*Dll4*^{i3COIN} and littermate-control mice. **h**, Percentage (control, $n = 10$; VE-Cad^{creER}-*Dll4*^{i3COIN}, $n = 10$) of HSCs, MPP2 cells, MPP3–4 cells, MPP4 cells and LSK cells from the bone marrow of VE-Cad^{creER}-*Dll4*^{i3COIN} and littermate-control mice. **i**, Total numbers of bone marrow HSCs, MPP2 cells, MPP3 cells, MPP4 cells and LSK cells from VE-Cad^{creER}-*Dll4*^{i3COIN} and littermate-control mice (control, $n = 10$; VE-Cad^{creER}-*Dll4*^{i3COIN}, $n = 10$). **j**, Representative immunofluorescence of early progenitors (Lin^{-}CD48^{-}CD150^{+}) adjacent to the DLL4-producing vascular endothelium in *Dll4-mCherry*. Lin cocktail, CD11b, GR1, CD41, TER119 and B220. Arrowhead, Lin^{-}CD150^{+} progenitors. $n = 3$ mice. **k**, scRNA-seq *t*-SNE visualization of the LSK compartment ($n = 21{,}116$ cells), colour-coded by genotype. **l, m**, Distribution of enrichment scores for myeloid progenitor (**l**) and HSC (**m**) gene signatures within the scRNA-seq-profiled HSPC populations from bone marrow of tamoxifen-treated VE-Cad^{creER}-*Dll4*^{i3COIN} mice (pooled $n = 2$) and littermate-control mice (pooled $n = 2$). $n = 21{,}116$ cells. The data are mean ± s.d. NS, not significant, $*P \leq 0.05$, $**P \leq 0.01$, $***P \leq 0.001$, Student's *t*-test, two-tailed (**a–d, g–i**) or Wilcoxon rank-sum test (**l, m**). Data are representative of four (**a–e**) or two (**g**) independent experiments.

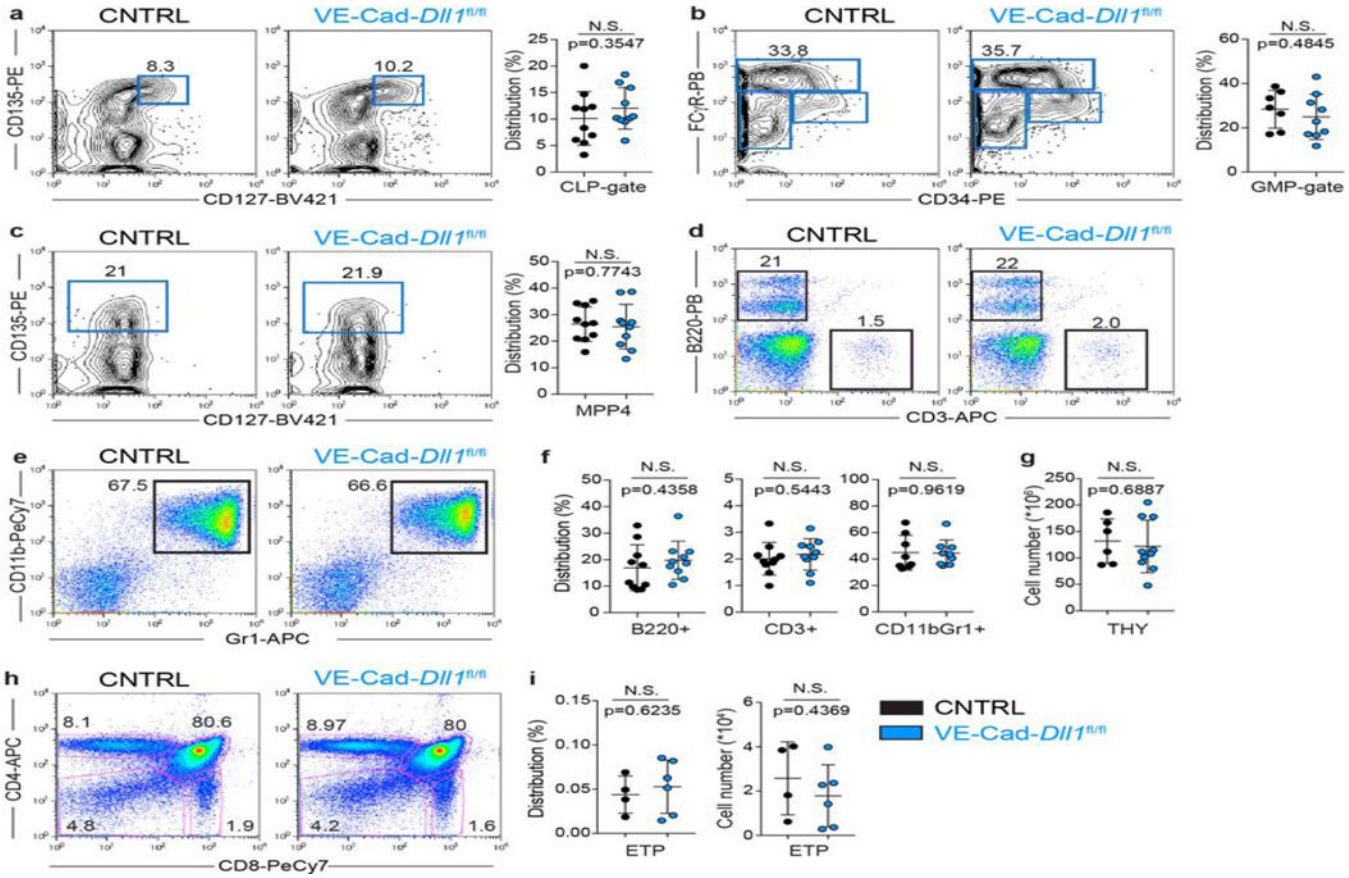

Extended Data Figure 10: Deletion of endothelial *Dll1* does not affect early lineage priming of haematopoietic progenitors.

a–f, Flow cytometry analysis of bone marrow progenitors in VE-Cad-*Dll1*$^{fl/fl}$ and littermate-control mice, showing equivalent frequencies of common lymphoid progenitors (control, n = 10; VE-Cad-*Dll1*$^{fl/fl}$, n = 8) (**a**), granulocyte–monocyte progenitors (control, n = 7; VE-Cad-*Dll1*$^{fl/fl}$, n = 9) (**b**) and MPP4 cells (control, n = 10; VE-Cad-*Dll1*$^{fl/fl}$, n = 10) (**c**), of B220^{+} B cells (control, n = 10; VE-Cad-*Dll1*$^{fl/fl}$, n = 10) (**d, f**), CD3^{+} T cells (control, n = 10; VE-Cad-*Dll1*$^{fl/fl}$, n = 10) (**d, f**) and CD11b^{+}GR1^{+} monocytic–granulocytic subset (control, n = 8; VE-Cad-*Dll1*$^{fl/fl}$, n = 9) (**e, f**). **g**, Absolute numbers of thymocytes from VE-Cad-*Dll1*$^{fl/fl}$ and littermate-control mice (control, n = 6; VE-Cad-*Dll1*$^{fl/fl}$, n = 10). **h**, Representative flow cytometry analysis of thymic subsets in VE-Cad-*Dll1*$^{fl/fl}$ and littermate-control mice. **i**, Frequencies (control, n = 4; VE-Cad-*Dll1*$^{fl/fl}$, n = 6) and absolute numbers (control, n = 4; VE-Cad-*Dll1*$^{fl/fl}$, n = 6) of early thymic progenitors from thymi of VE-Cad-*Dll1*$^{fl/fl}$ and littermate-control mice. The data are mean ± s.d. N.S., not significant, Student's t-test, two-tailed. Data are representative of three independent experiments.

Acknowledgements

We would like to thank the NYULMC High Performance Computing, Flow Cytometry, Genome Technology Center, Histopathology Core and the Microscopy Laboratory. This research was supported by the US National Institutes of Health (RO1CA202025, RO1CA202027) (I.A), (DK056638, HL069438, DK116312, DK112976 to P.S.F.), the Leukemia & Lymphoma Society (I.A., A.N.T), the Alex's Lemonade Stand Foundation for Childhood Cancer (I.A., A.N.T.), the ERC Advanced grant:European Research Council (AdG 339409, AngioBone) (R. H. A.),

the American Cancer Society (RSG-15–189-01-RMC to A.T.) and the St. Baldrick's Foundation (581357 to A.T.). This work is dedicated to the memory of my (I.A.) mentor Harald von Boehmer.

Main text references

1. Morrison SJ & Scadden DT The bone marrow niche for haematopoietic stem cells. Nature 505, 327–334, doi:10.1038/nature12984 (2014). [PubMed: 24429631]
2. Wei Q & Frenette PS Niches for Hematopoietic Stem Cells and Their Progeny. Immunity 48, 632–648, doi:10.1016/j.immuni.2018.03.024 (2018). [PubMed: 29669248]
3. Ding L & Morrison SJ Haematopoietic stem cells and early lymphoid progenitors occupy distinct bone marrow niches. Nature 495, 231–235, doi:10.1038/nature11885 (2013). [PubMed: 23434755]
4. Zhu J et al. Osteoblasts support B-lymphocyte commitment and differentiation from hematopoietic stem cells. Blood 109, 3706–3712, doi:10.1182/blood-2006-08-041384 (2007). [PubMed: 17227831]
5. Mendez-Ferrer S, Lucas D, Battista M & Frenette PS Haematopoietic stem cell release is regulated by circadian oscillations. Nature 452, 442–447, doi:10.1038/nature06685 (2008). [PubMed: 18256599]
6. Lucas D et al. Chemotherapy-induced bone marrow nerve injury impairs hematopoietic regeneration. Nat Med 19, 695–703, doi:10.1038/nm.3155 (2013). [PubMed: 23644514]
7. Chow A et al. Bone marrow CD 169+ macrophages promote the retention of hematopoietic stem and progenitor cells in the mesenchymal stem cell niche. J Exp Med 208, 261–271, doi:10.1084/jem.20101688 (2011). [PubMed: 21282381]
8. Bruns I et al. Megakaryocytes regulate hematopoietic stem cell quiescence through CXCL4 secretion. Nat Med 20, 1315–1320, doi:10.1038/nm.3707 (2014). [PubMed: 25326802]
9. Yamazaki S et al. Nonmyelinating Schwann cells maintain hematopoietic stem cell hibernation in the bone marrow niche. Cell 147, 1146–1158, doi:10.1016/j.cell.2011.09.053 (2011). [PubMed: 22118468]
10. Kusumbe AP, Ramasamy SK & Adams RH Coupling of angiogenesis and osteogenesis by a specific vessel subtype in bone. Nature 507, 323–328, doi:10.1038/nature13145 (2014). [PubMed: 24646994]
11. Zhou BO, Yue R, Murphy MM, Peyer JG & Morrison SJ Leptin-receptor-expressing mesenchymal stromal cells represent the main source of bone formed by adult bone marrow. Cell Stem Cell 15, 154–168, doi:10.1016/j.stem.2014.06.008 (2014). [PubMed: 24953181]
12. Mizoguchi T et al. Osterix marks distinct waves of primitive and definitive stromal progenitors during bone marrow development. Dev Cell 29, 340–349, doi:10.1016/j.devcel.2014.03.013 (2014). [PubMed: 24823377]
13. Butler A, Hoffman P, Smibert P, Papalexi E & Satija R Integrating single-cell transcriptomic data across different conditions, technologies, and species. Nat Biotechnol 36, 411–420, doi:10.1038/nbt.4096 (2018). [PubMed: 29608179]
14. Ramasamy SK Structure and Functions of Blood Vessels and Vascular Niches in Bone. Stem Cells Int 2017, 5046953, doi:10.1155/2017/5046953 (2017).
15. Xu C et al. Stem cell factor is selectively secreted by arterial endothelial cells in bone marrow. Nat Commun 9, 2449, doi:10.1038/s41467-018-04726-3 (2018). [PubMed: 29934585]
16. Hooper AT et al. Engraftment and reconstitution of hematopoiesis is dependent on VEGFR2-mediated regeneration of sinusoidal endothelial cells. Cell Stem Cell 4, 263–274, doi:10.1016/j.stem.2009.01.006 (2009). [PubMed: 19265665]
17. Nombela-Arrieta C et al. Quantitative imaging of haematopoietic stem and progenitor cell localization and hypoxic status in the bone marrow microenvironment. Nat Cell Biol 15, 533–543, doi:10.1038/ncb2730 (2013). [PubMed: 23624405]
18. Friedenstein AJ, Petrakova KV, Kurolesova AI & Frolova GP Heterotopic of bone marrow. Analysis of precursor cells for osteogenic and hematopoietic tissues. Transplantation 6, 230–247 (1968). [PubMed: 5654088]

19. Ghazanfari R, Li H, Zacharaki D, Lim HC & Scheding S Human Non-hematopoietic CD271(pos)/CD140a(low/neg) Bone Marrow Stroma Cells Fulfill Stringent Stem Cell Criteria in Serial Transplantations. Stem Cells Dev, doi:10.1089/scd.2016.0169 (2016).
20. Mitroulis I et al. Secreted protein Del-1 regulates myelopoiesis in the hematopoietic stem cell niche. J Clin Invest 127, 3624–3639, doi:10.1172/JCI92571 (2017). [PubMed: 28846069]
21. Yang G et al. Osteogenic fate of hypertrophic chondrocytes. Cell Res 24, 1266–1269, doi:10.1038/cr.2014.111 (2014). [PubMed: 25145361]
22. Crane GM, Jeffery E & Morrison SJ Adult haematopoietic stem cell niches. Nat Rev Immunol 17, 573–590, doi:10.1038/nri.2017.53 (2017). [PubMed: 28604734]
23. Winkler IG et al. Vascular niche E-selectin regulates hematopoietic stem cell dormancy, self renewal and chemoresistance. Nat Med 18, 1651–1657, doi:10.1038/nm.2969 (2012). [PubMed: 23086476]
24. Cordeiro Gomes A et al. Hematopoietic Stem Cell Niches Produce Lineage-Instructive Signals to Control Multipotent Progenitor Differentiation. Immunity 45, 1219–1231, doi:10.1016/j.immuni.2016.11.004 (2016). [PubMed: 27913094]
25. Mrozek E, Anderson P & Caligiuri MA Role of interleukin-15 in the development of human CD56+ natural killer cells from CD34+ hematopoietic progenitor cells. Blood 87, 2632–2640 (1996). [PubMed: 8639878]
26. Goldman DC et al. BMP4 regulates the hematopoietic stem cell niche. Blood 114, 4393–4401, doi:10.1182/blood-2009-02-206433 (2009). [PubMed: 19759357]
27. Shi C et al. Bone marrow mesenchymal stem and progenitor cells induce monocyte emigration in response to circulating toll-like receptor ligands. Immunity 34, 590–601, doi:10.1016/j.immuni.2011.02.016 (2011). [PubMed: 21458307]
28. Nemeth MJ, Topol L, Anderson SM, Yang Y & Bodine DM Wnt5a inhibits canonical Wnt signaling in hematopoietic stem cells and enhances repopulation. Proc Natl Acad Sci U S A 104, 15436–15441, doi:10.1073/pnas.0704747104 (2007). [PubMed: 17881570]
29. Smith GD, Gunnell D & Holly J Cancer and insulin-like growth factor-I. A potential mechanism linking the environment with cancer risk. BMJ 321, 847–848 (2000). [PubMed: 11021847]
30. Yu VW et al. Distinctive Mesenchymal-Parenchymal Cell Pairings Govern B Cell Differentiation in the Bone Marrow. Stem Cell Reports 7, 220–235, doi:10.1016/j.stemcr.2016.06.009 (2016). [PubMed: 27453006]
31. Mauch P et al. Hematopoietic stem cell compartment: acute and late effects of radiation therapy and chemotherapy. Int J Radiat Oncol Biol Phys 31, 1319–1339, doi:10.1016/0360-3016(94)00430-S (1995). [PubMed: 7713791]
32. Herault A et al. Myeloid progenitor cluster formation drives emergency and leukaemic myelopoiesis. Nature 544, 53–58, doi:10.1038/nature21693 (2017). [PubMed: 28355185]
33. Zhou BO et al. Bone marrow adipocytes promote the regeneration of stem cells and haematopoiesis by secreting SCF. Nat Cell Biol 19, 891–903, doi:10.1038/ncb3570 (2017). [PubMed: 28714970]
34. Van Zant G Studies of hematopoietic stem cells spared by 5-fluorouracil. J Exp Med 159, 679–690 (1984). [PubMed: 6699542]
35. Klinakis A et al. A novel tumour-suppressor function for the Notch pathway in myeloid leukaemia. Nature 473, 230–233, doi:10.1038/nature09999 (2011). [PubMed: 21562564]
36. Song R et al. Mind bomb 1 in the lymphopoietic niches is essential for T and marginal zone B cell development. JExp Med 205, 2525–2536, doi:10.1084/jem.20081344 (2008). [PubMed: 18824586]
37. Poulos MG et al. Endothelial Jagged-1 is necessary for homeostatic and regenerative hematopoiesis. Cell Rep 4, 1022–1034, doi:10.1016/j.celrep.2013.07.048 (2013). [PubMed: 24012753]
38. Koch U et al. Delta-like 4 is the essential, nonredundant ligand for Notch1 during thymic T cell lineage commitment. J Exp Med 205, 2515–2523, doi:10.1084/jem.20080829 (2008). [PubMed: 18824585]

39. Schmitt TM, Ciofani M, Petrie HT & Zuniga-Pflucker JC Maintenance of T cell specification and differentiation requires recurrent notch receptor-ligand interactions. J Exp Med 200, 469–479, doi:10.1084/jem.20040394 (2004). [PubMed: 15314075]

40. Lehar SM, Dooley J, Farr AG & Bevan MJ Notch ligands Delta 1 and Jagged1 transmit distinct signals to T-cell precursors. Blood 105, 1440–1447, doi:10.1182/blood-2004-08-3257 (2005). [PubMed: 15486060]

41. Olsson A et al. Single-cell analysis of mixed-lineage states leading to a binary cell fate choice. Nature 537, 698–702, doi:10.1038/nature19348 (2016). [PubMed: 27580035]

42. Paul F et al. Transcriptional Heterogeneity and Lineage Commitment in Myeloid Progenitors. Cell 163, 1663–1677, doi:10.1016/j.cell.2015.11.013 (2015). [PubMed: 26627738]

43. Pronk CJ et al. Elucidation of the phenotypic, functional, and molecular topography of a myeloerythroid progenitor cell hierarchy. Cell Stem Cell 1, 428–442, doi:10.1016/j.stem.2007.07.005 (2007). [PubMed: 18371379]

44. Ng SY, Yoshida T, Zhang J & Georgopoulos K Genome-wide lineage-specific transcriptional networks underscore Ikaros-dependent lymphoid priming in hematopoietic stem cells. Immunity 30, 493–507, doi:10.1016/j.immuni.2009.01.014 (2009). [PubMed: 19345118]

45. Acar M et al. Deep imaging of bone marrow shows non-dividing stem cells are mainly perisinusoidal. Nature 526, 126–130, doi:10.1038/nature15250 (2015). [PubMed: 26416744]

46. Pietras EM et al. Functionally Distinct Subsets of Lineage-Biased Multipotent Progenitors Control Blood Production in Normal and Regenerative Conditions. Cell Stem Cell 17, 35–46, doi:10.1016/j.stem.2015.05.003 (2015). [PubMed: 26095048]

47. Giladi A et al. Single-cell characterization of haematopoietic progenitors and their trajectories in homeostasis and perturbed haematopoiesis. Nat Cell Biol 20, 836–846, doi:10.1038/s41556-018-0121-4 (2018). [PubMed: 29915358]

48. Jacobsen SEW & Nerlov C Haematopoiesis in the era of advanced single-cell technologies. Nat Cell Biol 21, 2–8, doi:10.1038/s41556-018-0227-8 (2019). [PubMed: 30602765]

49. Passaro D et al. CXCR4 Is Required for Leukemia-Initiating Cell Activity in T Cell Acute Lymphoblastic Leukemia. Cancer Cell 27, 769–779, doi:10.1016/j.ccell.2015.05.003 (2015). [PubMed: 26058076]

50. Pitt LA et al. CXCL12-Producing Vascular Endothelial Niches Control Acute T Cell Leukemia Maintenance. Cancer Cell 27, 755–768, doi:10.1016/j.ccell.2015.05.002 (2015). [PubMed: 26058075]

REFERENCES

51. Alva JA et al. VE-Cadherin-Cre-recombinase transgenic mouse: a tool for lineage analysis and gene deletion in endothelial cells. Dev Dyn 235, 759–767, doi:10.1002/dvdy.20643 (2006). [PubMed: 16450386]

52. DeFalco J et al. Virus-assisted mapping of neural inputs to a feeding center in the hypothalamus. Science 291, 2608–2613, doi:10.1126/science.1056602 (2001). [PubMed: 11283374]

53. Kim JE, Nakashima K & de Crombrugghe B Transgenic mice expressing a ligand-inducible cre recombinase in osteoblasts and odontoblasts: a new tool to examine physiology and disease of postnatal bone and tooth. Am J Pathol 165, 1875–1882, doi:10.1016/S0002-9440(10)63240-3 (2004). [PubMed: 15579432]

54. Madisen L et al. A robust and high-throughput Cre reporting and characterization system for the whole mouse brain. Nat Neurosci 13, 133–140, doi:10.1038/nn.2467 (2010). [PubMed: 20023653]

55. Economides AN et al. Conditionals by inversion provide a universal method for the generation of conditional alleles. Proc Natl Acad Sci USA 110, E3179–3188, doi:10.1073/pnas.1217812110 (2013). [PubMed: 23918385]

56. Hozumi K et al. Delta-like 1 is necessary for the generation of marginal zone B cells but not T cells in vivo. Nat Immunol 5, 638–644, doi:10.1038/ni1075 (2004). [PubMed: 15146182]

57. Lee EC et al. A highly efficient Escherichia coli-based chromosome engineering system adapted for recombinogenic targeting and subcloning of BAC DNA. Genomics 73, 56–65, doi:10.1006/geno.2000.6451 (2001). [PubMed: 11352566]

58. Reizis B & Leder P The upstream enhancer is necessary and sufficient for the expression of the pre-T cell receptor alpha gene in immature T lymphocytes. J Exp Med 194, 979–990 (2001). [PubMed: 11581319]
59. Dobin A et al. STAR: ultrafast universal RNA-seq aligner. Bioinformatics 29, 15–21, doi:10.1093/bioinformatics/bts635 (2013). [PubMed: 23104886]
60. Liao Y, Smyth GK & Shi W featureCounts: an efficient general purpose program for assigning sequence reads to genomic features. Bioinformatics 30, 923–930, doi:10.1093/bioinformatics/btt656 (2014). [PubMed: 24227677]
61. Love MI, Huber W & Anders S Moderated estimation of fold change and dispersion for RNA-seq data with DESeq2. Genome Biol 15, 550, doi:10.1186/s13059-014-0550-8 (2014). [PubMed: 25516281]
62. Zheng GX et al. Massively parallel digital transcriptional profiling of single cells. Nat Commun 8, 14049, doi:10.1038/ncomms14049 (2017). [PubMed: 28091601]
63. Macosko EZ et al. Highly Parallel Genome-wide Expression Profiling of Individual Cells Using Nanoliter Droplets. Cell 161, 1202–1214, doi:10.1016/j.cell.2015.05.002 (2015). [PubMed: 26000488]
64. Mayer C et al. Developmental diversification of cortical inhibitory interneurons. Nature 555, 457–462, doi:10.1038/nature25999 (2018). [PubMed: 29513653]
65. Rodda LB et al. Single-Cell RNA Sequencing of Lymph Node Stromal Cells Reveals Niche-Associated Heterogeneity. Immunity 48, 1014–1028 e1016, doi:10.1016/j.immuni.2018.04.006 (2018). [PubMed: 29752062]
66. Finak G et al. MAST: a flexible statistical framework for assessing transcriptional changes and characterizing heterogeneity in single-cell RNA sequencing data. Genome Biol 16, 278, doi:10.1186/s13059-015-0844-5 (2015). [PubMed: 26653891]
67. Tirosh I et al. Dissecting the multicellular ecosystem of metastatic melanoma by single-cell RNA-seq. Science 352, 189–196, doi:10.1126/science.aad0501 (2016). [PubMed: 27124452]
68. Trapnell C et al. The dynamics and regulators of cell fate decisions are revealed by pseudotemporal ordering of single cells. Nat Biotechnol 32, 381–386, doi:10.1038/nbt.2859 (2014). [PubMed: 24658644]
69. Yu G, Wang LG, Han Y & He QY clusterProfiler: an R package for comparing biological themes among gene clusters. OMICS 16, 284–287, doi:10.1089/omi.2011.0118 (2012). [PubMed: 22455463]
70. Chen EY et al. Enrichr: interactive and collaborative HTML5 gene list enrichment analysis tool. BMC Bioinformatics 14, 128, doi:10.1186/1471-2105-14-128 (2013). [PubMed: 23586463]

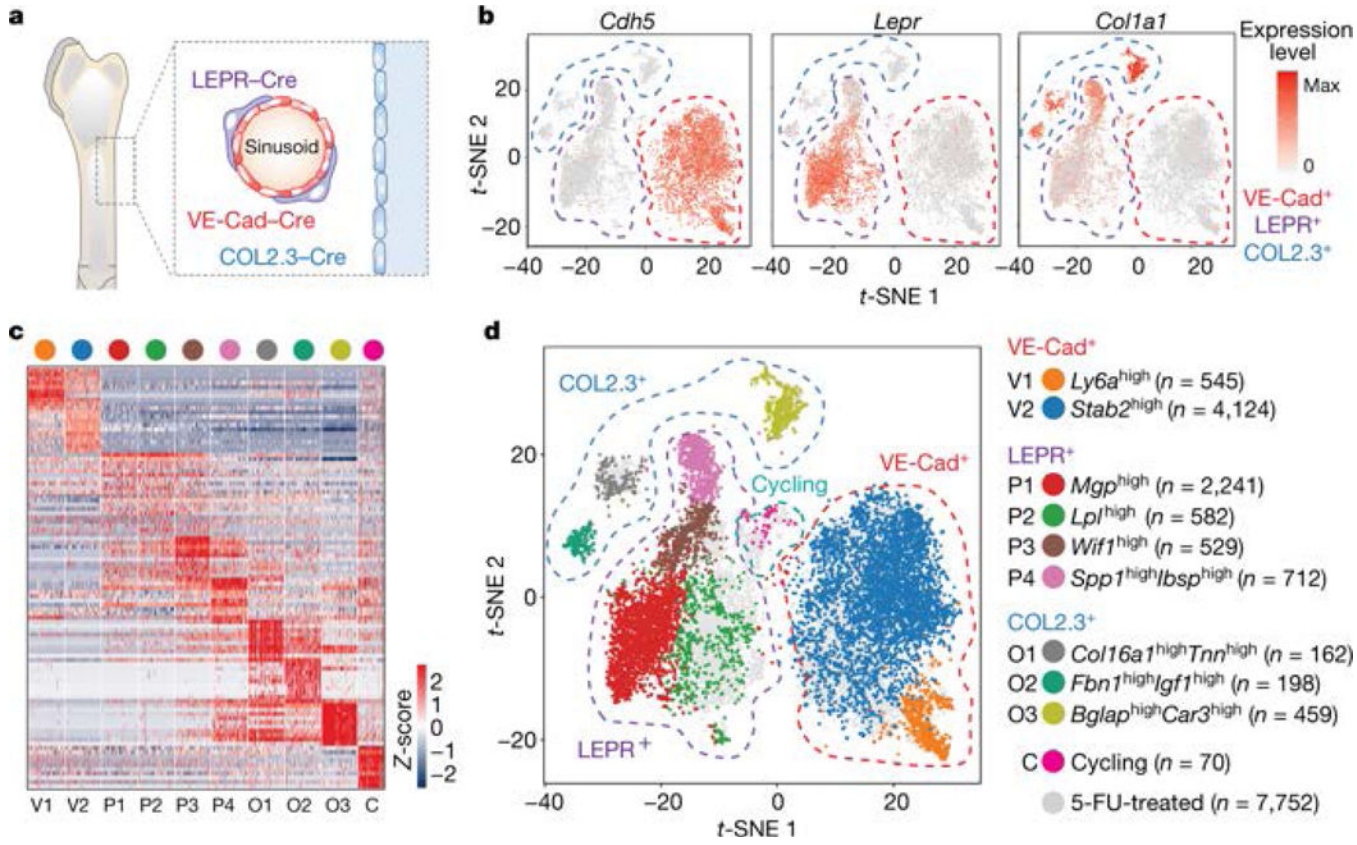

Figure 1: Single-cell RNA-sequencing analysis of the BM microenvironment at steady state.

a, Schematic representation of BM niche: osteoblasts (Col2.3$^+$, blue), perivascular LepR$^+$ (LepR$^+$, purple), and vascular cells (VEcad$^+$, red). **b**. Expression levels of genes associated with niche-specific Cre strains, including *Cdh5* (VE-cadherin), *Lepr* (Leptin receptor) and *Col1a1* (Col2.3) overlaid on tSNE representation (n=9,622 cells). Dashed lines generally encompass the cells profiled in Col2.3$^+$, LepR$^+$, VEcad$^+$ libraries. **c**, Gene signatures of VEcad$^+$, LepR$^+$, and Col2.3$^+$ sub-populations based on the relative expression levels of the 10 most significant markers for each of the 10 clusters, displaying 100 randomly-selected cells per cluster. MAST with Bonferroni correction. **d**, tSNE visualization of color-coded clustering of BM niche (n=17,374 cells). Dashed lines generally encompass the examined VEcad$^+$ (red), LepR$^+$ (purple), Col2.3$^+$ (blue) BM niche populations and the cycling cells (sea green).

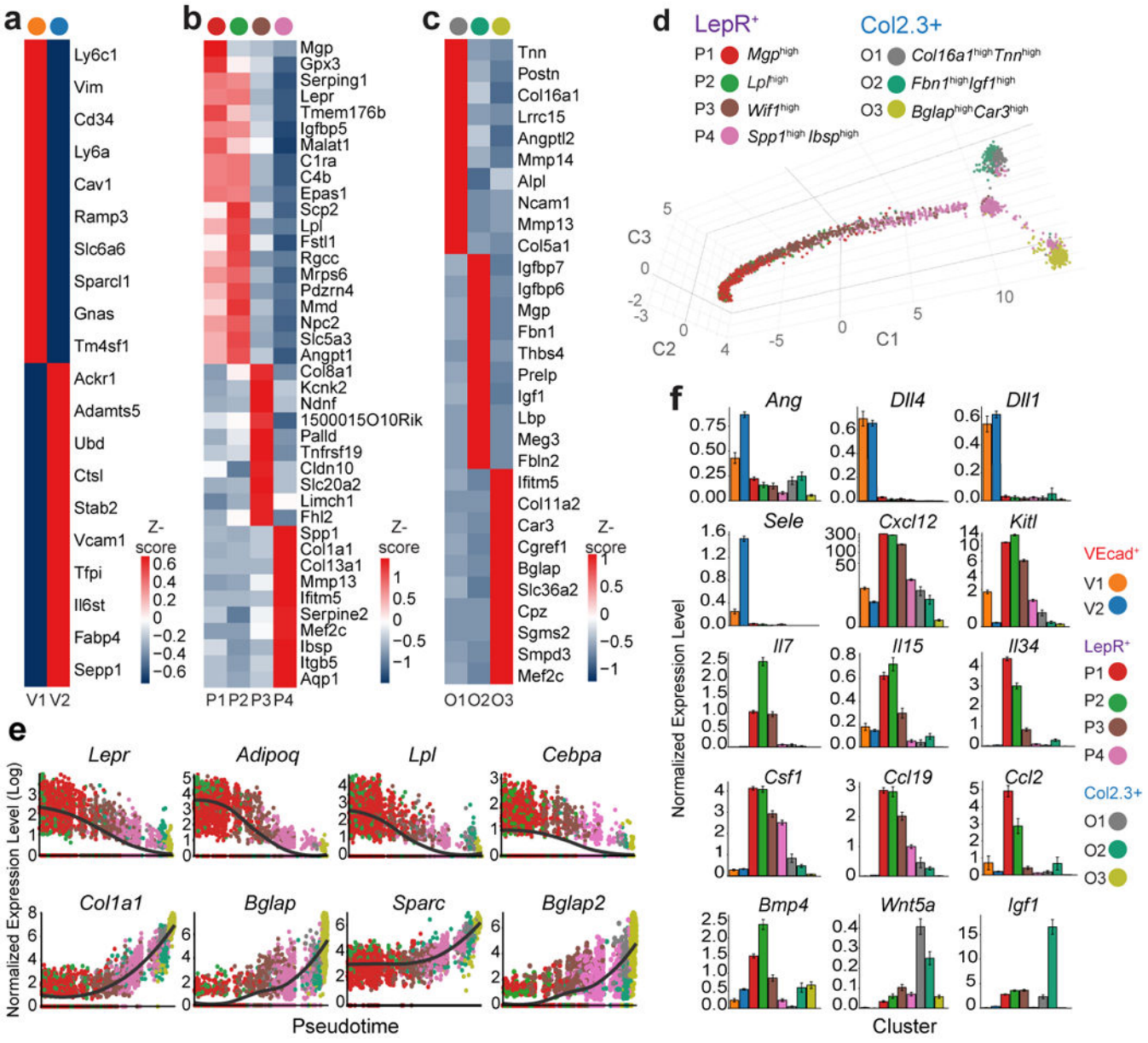

Figure 2: Expression of pro-hematopoietic factors by the BM microenvironment.

a-c, Gene signatures of BM niche sub-populations based on the average relative expression levels of the 10 most significant markers for each cluster exclusively within the parent niche subsets (VEcad$^+$ (**a**), LepR$^+$(**b**), or Col2.3$^+$(**c**)) at steady state. MAST with Bonferroni correction. **d**, Reconstructed cell differentiation trajectory of LepR$^+$ and Col2.3$^+$ clusters colored by subpopulation identity. **e**, Expression levels of indicated genes in LepR$^+$ and Col2.3$^+$ cells with respect to their pseudotime coordinates. Black lines depict the LOESS fit of the normalized expression values. **f**, Expression levels of pro-hematopoietic factors in the non-cycling clusters (n=9,622 cells). The data are mean ± standard error.

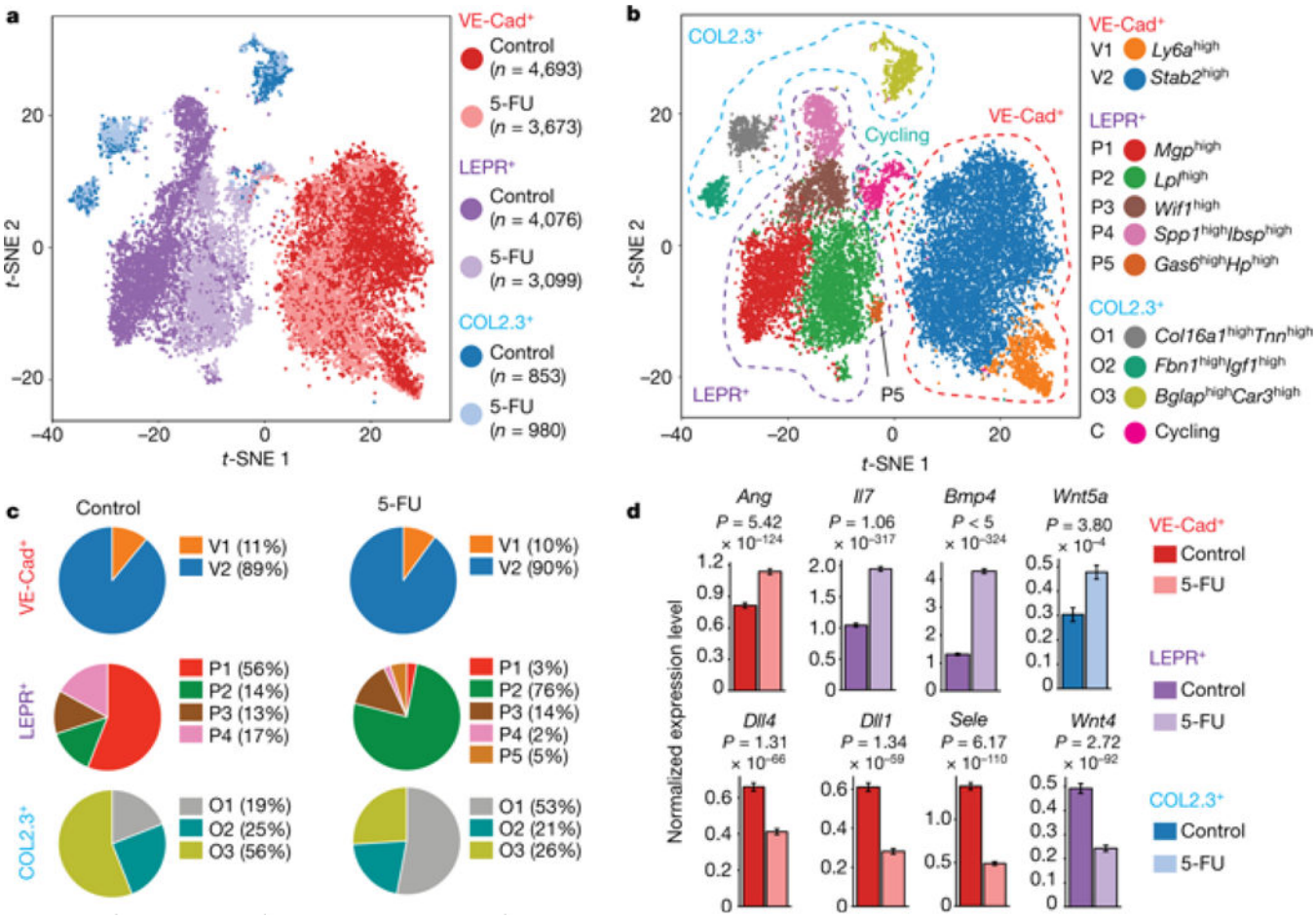

Figure 3: Single-cell transcriptome profiling of the BM niche in response to chemotherapy.

a, VEcad$^+$ (red), LepR$^+$ (purple), and Col2.3$^+$ (blue) cells at steady state (dark) or following 5-FU treatment (light) overlaid on tSNE representation (n=17,374 cells). **b**, tSNE plot of color-coded clusters of all examined (control and 5-FU treated) BM niche cells (n=17,374 cells). Dashed lines generally encompass the examined VEcad$^+$ (red), LepR$^+$(purple), Col2.3$^+$ (blue) BM niche populations and the cycling cells (sea green). **c**, Frequencies of each sub-population within VEcad$^+$, LepR$^+$, and Col2.3$^+$ compartments under the indicated condition. **d**, Relative expression of pro-hematopoietic factors examined in Fig. 2e in response to 5-FU treatment (n=17,374 cells). Adjusted *$P \leq 0.05$, **$P \leq 0.01$, ***$P < 0.001$ (MAST with Bonferroni correction). The data are mean ± standard error.

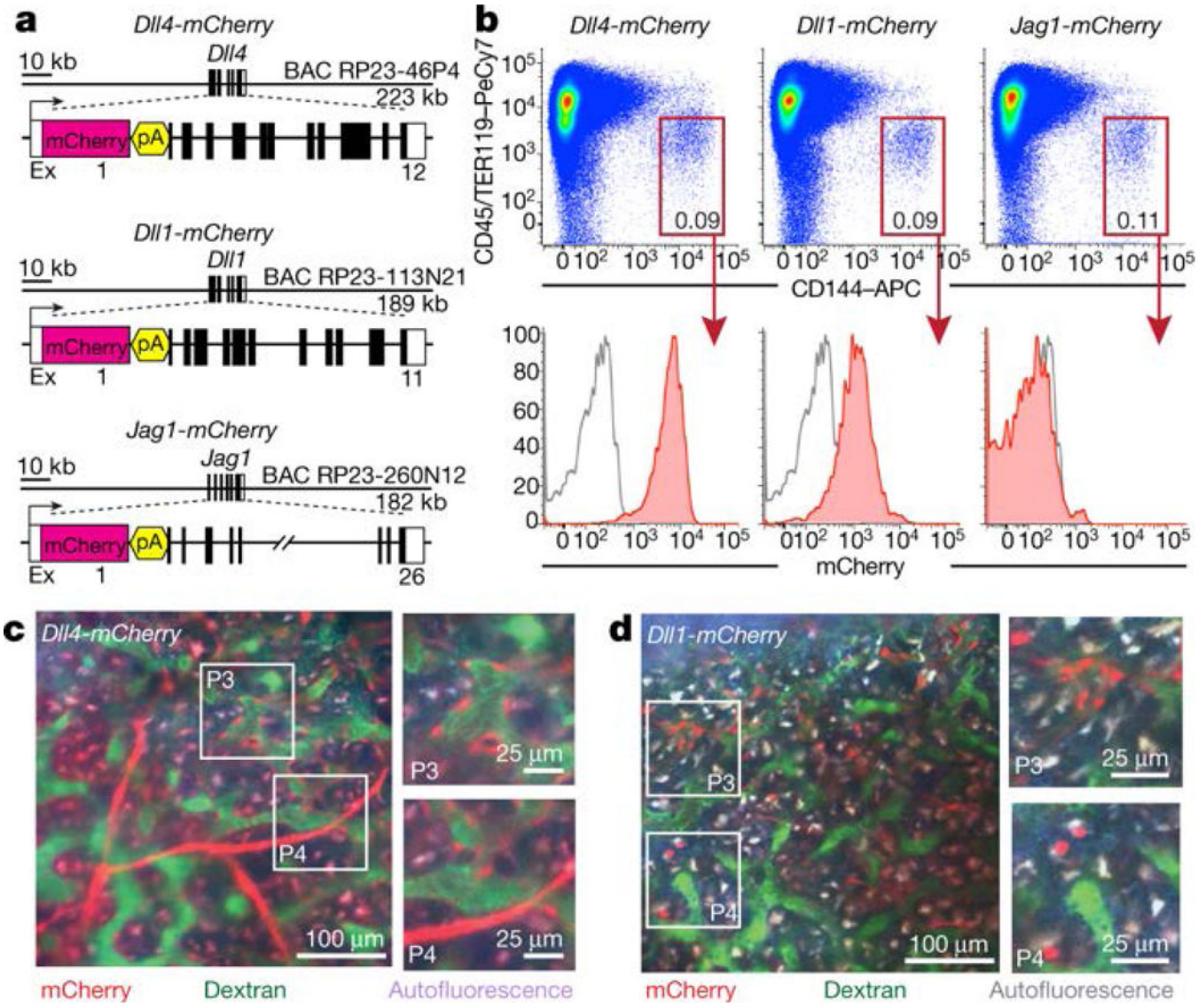

Figure 4: Vascular endothelial cells are the major source of *Dll4* and *Dll1* in the BM.

a, Map of BAC clones used to drive transgenes *mDll4-mCherry*, *mDll1-mCherry*, and *mJag1-mCherry*. **b**, Representative flow cytometry histogram measuring mCherry fluorescence in DAPI^{-}CD45/Ter119^{low}CD144^{+} endothelial cells from BM of *mDll4-mCherry*, *mDll1-mCherry*, and *mJAG1-mCherry*. Indicated values represent percentages of the complete CD45/Ter119 population. **c-d**, Representative two photon images of BM from dextran-injected *mDll4-mCherry* (**c**) and *mDll1-mCherry* (**d**). (**c-d**) Scale bars are 100 µm and 25 µm, as indicated in the images. Data are representative of three independent experiments (**b-d**).

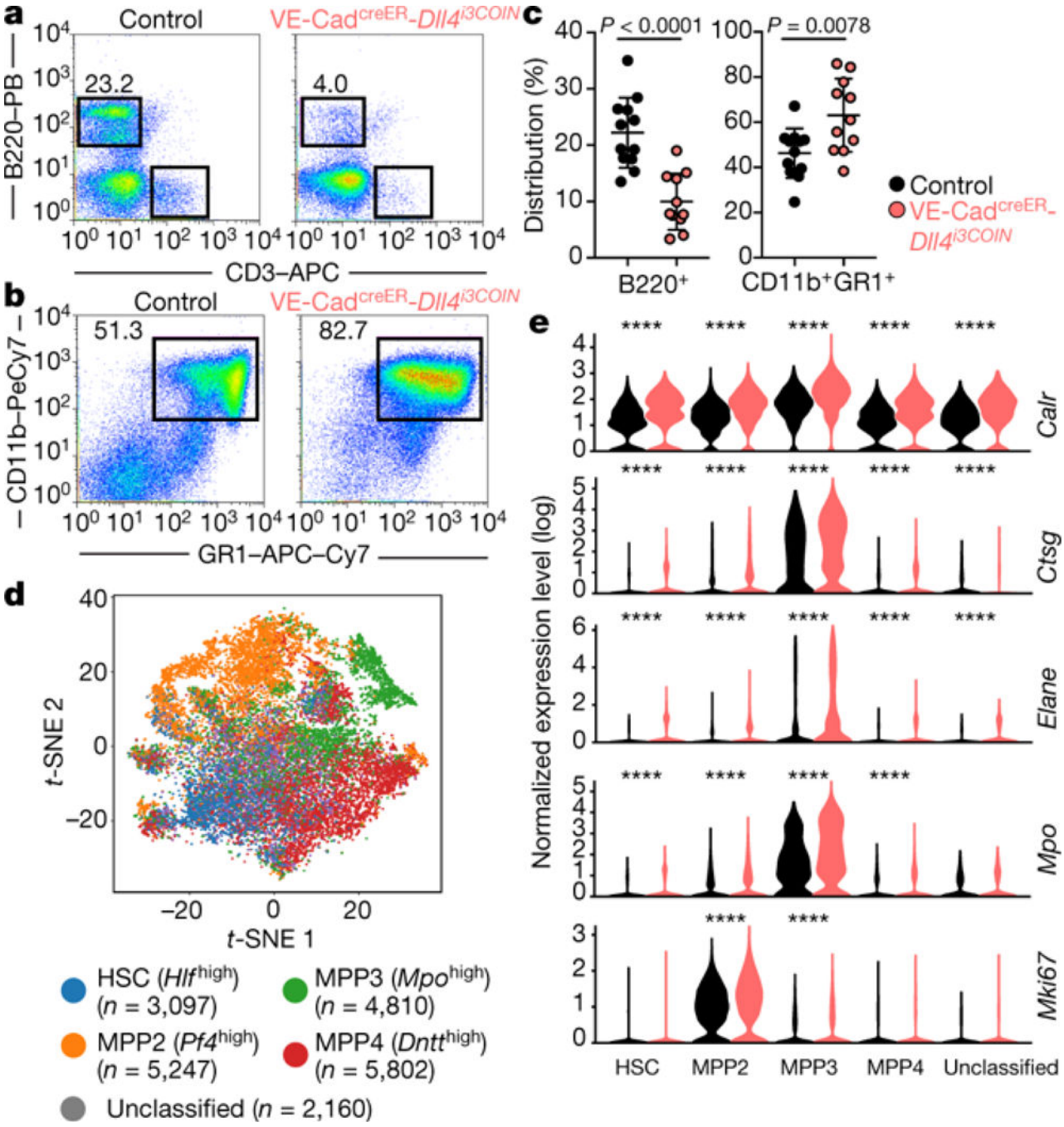

Figure 5: Dll4 expressed by vascular endothelial cells prevents myeloid skewing of hematopoietic progenitors.

a-c, Representative flow cytometry (**a,b**) and frequencies (**c**) of mature hematopoietic subsets in VEc-*Dll4*^{i3COIN} and littermate control animals, including B220^{+} B cells (CNTRL: n=12; VEc-*Dll4*^{i3COIN}: n=11) and CD11b^{+}Gr1^{+} cells (CNTRL: n=12; VEc-*Dll4*^{i3COIN}: n=11). **d**, LSK compartment scRNA-seq tSNE visualization (n=21,116 cells), color-coded by the identified HSPC populations. **e**, Log-transformed normalized expression levels of myeloid-associated genes (*Calr*, *Ctsg*, *Elane*, and *Mpo*) and *Mki67* across HSPC populations

in control and VEc-*Dll4*^{i3COIN} LSK cells (n=21,116 cells). Violin plots depict kernel density estimation to show the distribution of expression values. Data are mean ± s.d. *$P \leq 0.05$, **$P \leq 0.01$, ***$P \leq 0.001$ (Student t-test, two-tailed (**c**), MAST test with Bonferroni correction (**e**)). Data are representative of four (**a-c**) independent experiments.